Inversion in optical imaging through atmospheric turbulence

Laurent Mugnier, Guy Le Besnerais and Serge Meimon

from « Inversion in optical imaging through atmospheric turbulence », chap. 10 of *Bayesian Approach to Inverse Problems*, edited by J. Idier, ISTE / John Wiley, 2008

Contents

10 Inversion in optical imaging through atmospheric turbulence **2**
10.1 Optical imaging through turbulence 2
10.1.1 Introduction 2
10.1.2 Image formation 3
10.1.2.1 Diffraction 3
10.1.2.2 Principle of optical interferometry 3
10.1.3 Effect of turbulence on image formation 4
10.1.3.1 Turbulence and phase 4
10.1.3.2 Long-exposure imaging 5
10.1.3.3 Short-exposure imaging 5
10.1.3.4 Case of a long-baseline interferometer 6
10.1.4 Imaging techniques 7
10.1.4.1 Speckle techniques 7
10.1.4.2 Deconvolution from wavefront sensing (DWFS) . . 7
10.1.4.3 Adaptive optics 8
10.1.4.4 Optical interferometry 8
10.2 Inversion approach and regularization criteria used 10
10.3 Measurement of aberrations 11
10.3.1 Introduction 11
10.3.2 Hartmann-Shack sensor 12
10.3.3 Phase retrieval and phase diversity 14
10.4 Myopic restoration in imaging 14
10.4.1 Motivation and noise statistic 14
10.4.2 Data processing in deconvolution from wavefront sensing . . 15
10.4.2.1 Conventional processing of short-exposure images . 15
10.4.2.2 Myopic deconvolution of short-exposure images . . 16
10.4.2.3 Simulations 17
10.4.2.4 Experimental results 18
10.4.3 Restoration of images corrected by adaptive optics 19
10.4.3.1 Myopic deconvolution of images corrected by AO . 19
10.4.3.2 Experimental results 20
10.4.4 Conclusion 22
10.5 Image reconstruction in optical interferometry (OI) 23
10.5.1 Observation model 23
10.5.2 Traditional Bayesian approach 25
10.5.3 Myopic modeling 26
10.5.4 Results 27
10.5.4.1 Processing of synthetic data 27
10.5.4.2 Processing of experimental data 29

Chapter 10

Inversion in optical imaging through atmospheric turbulence

from *Bayesian Approach to Inverse Problems*,
edited by J. Idier, ISTE / John Wiley, 2008

10.1 Optical imaging through turbulence

10.1.1 Introduction

The theoretical resolving power of a telescope is limited by its diameter. In real instruments, this theoretical limit, called the diffraction-limit resolution, often cannot be reached because of the presence of optical aberrations. These aberrations may come from the telescope itself or from the light wave propagation medium. In the case of ground-based astronomy, aberrations are mostly due to atmospheric turbulence. Several techniques have been developed to improve the resolution of observation instruments and avoid the degradation caused by turbulence. In this section, we recall some essential ideas in optical imaging, in particular on the optical effects of turbulence, then review the various techniques of high-resolution imaging through turbulence.

Section 10.2 gives a brief presentation of the inversion approach and the regularization criteria used in this chapter. Section 10.3 is an introduction to wavefront sensors (WFSs) and the processing problems that arise from their use. WFSs are devices that measure optical aberrations and are essential components of many high resolution optical imaging instruments today.

Three imaging techniques are illustrated by the inverse problems associated with them. These inverse problems are: image restoration for deconvolution from wavefront sensing and for imaging using adaptive optics, discussed in section 10.4, and image reconstruction for optical interferometry (section 10.5).

Chapter written by Laurent MUGNIER, Guy LE BESNERAIS and Serge MEIMON.
Laurent Mugnier and Serge Meimon are grateful to their colleagues of the High Angular Resolution team and particularly to its successive leaders Marc Séchaud and Vincent Michau, who created and maintained a stimulating team spirit made up of intellectual curiosity and a desire to share knowledge. With special thanks from Laurent Mugnier for the discussions with Jean-Marc Conan that introduced him to this field and from Serge Meimon for his talks with Frédéric Cassaing.

10.1.2 Image formation

10.1.2.1 Diffraction

Image formation is well described by the scalar theory of diffraction, presented in detail in reference works such as [Goo68, BW93]. A modern introductory overview can be found in [Mar89]. Image formation can be modeled by a convolution, at least within the instrument's so-called isoplanatic patch. At visible wavelengths, this patch is typically of the order of a degree when only aberrations due to the telescope itself are considered and a few arcseconds (1 arcsec $= 1/3\,600°$) for a telescope observing space through turbulence.

The instantaneous point-spread function (PSF) of a telescope or "telescope + atmosphere" system is equal to the square modulus of the Fourier transform (FT) of the complex amplitude of the field $\psi = P \exp(j\varphi)$ present in the aperture of the instrument when the object observed is a point source:

$$h(\boldsymbol{\xi}) = \left| \mathrm{FT}^{-1} \left(P(\lambda \boldsymbol{u})\, e^{j\varphi(\lambda \boldsymbol{u})} \right) \right|^2 (\boldsymbol{\xi}) \tag{10.1}$$

where λ is the imaging wavelength and imaging is assumed quasi-monochromatic. This PSF is conventionally normalized to a unit integral. In expression (10.1), the FT is the field transformation performed by the telescope between the pupil plane and the focal plane, and the square modulus is due to the detection being quadratic i.e., in intensity. Vector $\boldsymbol{\xi} = [\xi, \zeta]^T$ is composed of angles in the sky, in radians. For a perfect telescope in the absence of turbulence, P is constant in the aperture and φ is zero[1]. For a real telescope, the variations of the field $P \exp(j\varphi)$ are due both to aberrations belonging to the telescope and to those introduced by the turbulence.

In what follows, we assume that P is simply the aperture indicatrix, i.e., that the variations of intensity in the input pupil are negligible. This hypothesis is generally valid in astronomical imaging and is called the near-field approximation.

Equation (10.1) indicates that the optical transfer function, or OTF, is the autocorrelation of $\psi = P\, e^{j\varphi}$ dilated by the inverse of the wavelength, which is written

$$\widehat{h}(\boldsymbol{u}) = P\, e^{j\varphi} \otimes P\, e^{j\varphi}(\lambda \boldsymbol{u}). \tag{10.2}$$

In the absence of aberrations, i.e., when the phase φ is zero, the OTF is the autocorrelation of the aperture P. It has a spatial cut-off frequency equal to D/λ rad^{-1}, where D is the diameter of the aperture, and is strictly zero beyond it. The ultimate resolution of a telescope (sometimes called a monolithic telescope in contrast to the interferometers described below) is thus limited by its diameter D. Today's technology limits diameters to ten meters or so for ground-based telescopes and a few meters for telescopes on board satellites because of size and mass constraints. Optical interferometry (OI) is a technique that allows us to go beyond the resulting resolution limitation.

10.1.2.2 Principle of optical interferometry

This technique consists of taking the electromagnetic fields received at each of the apertures of an array of apertures (unit telescopes or mirror segments) and making them interfere. For each pair (k, ℓ) of apertures, the data contains high-resolution information at (or around) the angular spatial frequency $\boldsymbol{B}_{k,\ell}/\lambda$, where $\boldsymbol{B}_{k,\ell}$ is the vector

[1] The corresponding PSF is called the Airy pattern.

separating the apertures, or *baseline*. This spatial frequency can be much larger than the cut-off frequency D/λ of the individual apertures.

Depending on the type of interferometer and beam combination, it is possible either to form and measure an image of the object directly (the interferometer is then called an imaging interferometer) or to measure a discrete set of spatial frequencies of the object of interest (the interferometer can then be called a "correlation interferometer" as it measures the correlation of the electromagnetic fields between apertures [Cas97]). The reader interested in a more precise description of the different types of optical interferometers is invited to consult [RMCS01].

For a monolithic telescope, as for an interferometer, the transfer function is the autocorrelation of the input pupil (see equation (10.2)) provided that, if the interferometer is of the correlation type, the apertures are assimilated to points. For a long-baseline interferometer, i.e., when the baselines are large relative to the diameter of the individual apertures – which is generally the case for correlation interferometers – the difference between imaging and correlation interferometers becomes negligible as far as the information recorded in the data is concerned. The transfer functions of a monolithic telescope, an imaging interferometer and a correlation interferometer are illustrated in Figure 10.1. For an imaging interferometer, the processing required is, to a good

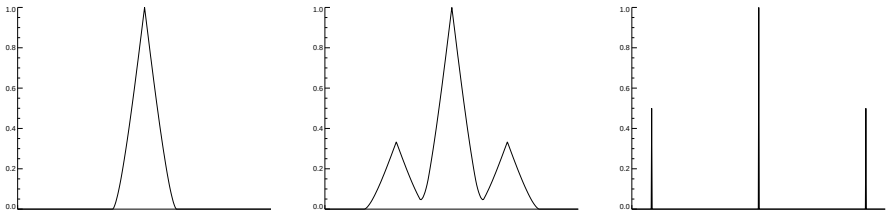

Figure 10.1: Cross-sections of transfer functions of a monolithic telescope (left), a three-telescope imaging interferometer (center) and a two-telescope correlation interferometer (right)

approximation, a deconvolution, with a PSF still given by equation (10.1) but more irregular than with a monolithic telescope because of the shape of the aperture.

For a correlation interferometer, the nature of the data processing problem changes: here, the aim is to reconstruct an object from Fourier coefficients, a problem called Fourier synthesis. This is the problem that will be tackled in section 10.5.

An intuitive way of representing data formation in a long-baseline interferometer is Young's double hole experiment, in which the aperture of each telescope is a (small) hole letting through the light coming from an object located at a great distance. Each pair (k, ℓ) of telescopes then gives a fringe pattern with a spatial frequency of $\boldsymbol{B}_{k,\ell}/\lambda$, where $\boldsymbol{B}_{k,\ell}$ is the vector linking telescopes k and ℓ. The contrasts and positions of these fringes can be measured and grouped together naturally in a number called the "complex visibility", which, in an ideal situation and in the absence of turbulence, gives the value of $\widehat{x}(\boldsymbol{B}_{k,\ell}/\lambda)/\widehat{x}(\boldsymbol{0})$ (Van Cittert-Zernike theorem [Goo85, Mar89]).

10.1.3 Effect of turbulence on image formation

10.1.3.1 Turbulence and phase

The inhomogeneities in the air temperature of the atmosphere generate inhomogeneities in the refractive index of the air, which perturb the propagation of light waves through

the atmosphere. These perturbations lead to space and time variations of the pupil phase φ, which can be modeled by a random process. In this section we recall a few results that enable the turbulent aperture phase to be modeled up to the second order. We will use the assumption, which is generally well verified, at least for scales of less than about ten meters, that the random variations of the refractive index of the air obey Kolmogorov's law: they follow a Gaussian probability law with zero mean and power spectral density (PSD) proportional to $|\boldsymbol{\nu}|^{-11/3}$, where $\boldsymbol{\nu}$ is the 3D spatial frequency [Rod81].

By integrating the phase along the optical path and in the framework of the near-field approximation, the spatial statistics of the phase in the telescope aperture can be deduced for a plane wave entering the atmosphere. The phase in the aperture is Gaussian since it is the result of the sum of all the index perturbations from the upper atmosphere down to the ground [Rod81]. The PSD of this phase is [Nol76]:

$$S_\varphi(\boldsymbol{u}) = 0.023\, r_0^{-5/3} u^{-11/3} \tag{10.3}$$

where $\boldsymbol{u}$ is the 2D spatial frequency in the aperture, u is its modulus, and r_0 is the key parameter quantifying the strength of the turbulence, called Fried's diameter [Fri65]. The smaller r_0, the stronger the turbulence. Typically, its value is about $10\,$cm in the visible range at a relatively good site.

The typical variation time τ of the turbulent phase in the aperture is given by the ratio of characteristic scale r_0 of this phase to mean wind speed Δv (which, more accurately, is a standard deviation of the distribution of the moduli of wind velocities [RGL82]):

$$\tau = r_0/\Delta v. \tag{10.4}$$

For $r_0 \simeq 10\,$cm and $\Delta v \simeq 10\,$m.s^{-1}, we obtain $\tau \simeq 10^{-2}\,$s. Thus, we talk about long exposures for images corresponding to an integration markedly longer than this time and short exposures for images with shorter integration times. For a full treatment of the time statistics of the turbulent phase, see [CRM95].

10.1.3.2 Long-exposure imaging

The turbulent long-exposure OTF is the product of the so-called static OTF, $\widehat{h^s}$, of the telescope without the atmosphere and an atmospheric transfer function, $\widehat{h^a}$, which has a cut-off frequency r_0/λ [Rod81]:

$$\widehat{h}(\boldsymbol{u}) \triangleq \langle \widehat{h}_t(\boldsymbol{u}) \rangle = \widehat{h^s}(\boldsymbol{u})\, \widehat{h^a}(\boldsymbol{u}) \text{ with } \widehat{h^a}(\boldsymbol{u}) = \exp\{-3.44\,(\lambda u/r_0)^{5/3}\}, \tag{10.5}$$

where the notation $\langle\cdot\rangle$ denotes a temporal mean over an arbitrarily long time. Thus we see that, for a telescope with a large diameter $D \gg r_0$, the long-exposure imaging resolution is limited by the turbulence and is no better than for a telescope of diameter r_0.

10.1.3.3 Short-exposure imaging

As noted by Labeyrie [Lab70], when the exposure time is short enough to freeze the turbulence (typically less than $10\,$ms, see equation (10.4)), the images retain the high-frequency information in the form of *speckles*, having a typical size λ/D and random positions. This is illustrated in Figure 10.2, which shows the simulated image of a star viewed through turbulence ($D/r_0 = 10$) using short (left) and long (right) exposures.

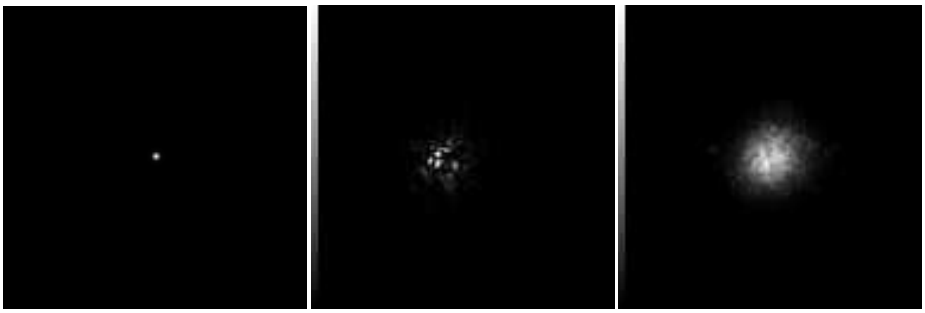

Figure 10.2: Images of a star simulated without atmospheric turbulence (left) and through turbulence (short exposure in center and long exposure on right). The strength of the turbulence is $D/r_0 = 10$. Image sampling respects Shannon's condition

It is possible to quantify the high-frequency information present in short-exposure images by evaluating the speckle transfer function (STF), defined as the second order moment of the instantaneous transfer function, $\langle|\widehat{h}_t(\boldsymbol{u})|^2\rangle$. For a large-diameter telescope ($D \gg r_0$), if we take an approximation on the turbulence statistics, we can find an approximate expression for the STF [Rod81]:

$$\langle|\widehat{h}_t(\boldsymbol{u})|^2\rangle \simeq \langle\widehat{h}_t(\boldsymbol{u})\rangle^2 + 0.435\,(r_0/D)^2\,\widehat{h}_0^s(\boldsymbol{u}) \tag{10.6}$$

where $\widehat{h}_0^s$ is the transfer function of a perfect telescope (i.e., with no aberration) of diameter D.

This expression allows us to describe the STF as the sum of the square of the long-exposure transfer function, which is low-frequency (LF), and a high-frequency (HF) component that extends up to the cut-off frequency of the telescope with an attenuation proportional to $(D/r_0)^2$. Thus, if we process a set of short-exposure images using a more judicious method than a simple average, it is possible to recover a high-resolution image of the observed object.

10.1.3.4 Case of a long-baseline interferometer

Equation (10.5) applies whatever the shape of the instrument's aperture and thus, in particular, applies to an interferometer. In a long exposure, the contrast of the fringes measured for a baseline $\boldsymbol{B}_{k,\ell}/\lambda$ is therefore multiplied by $\widehat{h^a}(\boldsymbol{B}_{k,\ell}/\lambda)$ and so strongly attenuated as to make the measurement of $\widehat{x}(\boldsymbol{B}_{k,\ell}/\lambda)$ unusable.

In a short exposure, for an interferometer where each aperture has a diameter smaller than the Fried diameter, r_0, or where turbulence is corrected using adaptive optics (see 10.1.4.3), the impact of turbulence on the interferometer measurements is easy to model: in the Young's holes analogy mentioned above, each hole k adds a phase shift (or piston) $\varphi_k(t)$ to the wave going through it, because of aberrations introduced by the turbulence in front of this aperture. The interference between two apertures k and ℓ are thus out of phase by the "differential piston" $\varphi_\ell(t) - \varphi_k(t)$, which, in a short exposure, is expressed by a random displacement of the fringes without attenuation of the contrast. The contrast attenuation in long exposures results from the averaging of these random displacements. Section 10.5 will present averaging techniques that get around the differential pistons. The short-exposure transfer function, at frequency

$\boldsymbol{B}_{k,\ell}/\lambda$, can be written:

$$\widehat{h}_t(\boldsymbol{B}_{k,\ell}/\lambda) = \eta_{k,\ell}(t)\, e^{j(\varphi_\ell(t)-\varphi_k(t))} \tag{10.7}$$

where $\eta_{k,\ell}(t)$ is a number that is often called the "instrumental visibility". In the absence of the many potential sources of visibility loss (residual perturbations of the wavefront at each telescope, differential tilts between telescopes, differential polarization effects, non-zero spectral width, etc.), the value of $\eta_{k,\ell}(t)$ is the inverse of the number of apertures interfering simultaneously (equation (10.2) considering that P is a sum of Dirac delta functions). In practice, this instrumental visibility is calibrated on a star known to be unresolved by the interferometer. Taking this calibration into account, we can thus replace $\eta_{k,\ell}(t)$ by 1 in equation (10.7).

Note that the measurement baseline $\boldsymbol{B}_{k,\ell}$ between apertures k and ℓ depends on time: the aperture configuration as seen from the object changes as the Earth rotates. This is used in "super-synthesis", a technique that consists, when the source emission does not vary in time, of repeating the measurements in the course of a night of observation to increase the frequency coverage of the interferometer.

10.1.4 Imaging techniques

The aim of high-resolution imaging through turbulence is to restore the HFs beyond the cut-off frequency r_0/λ of the long-exposure imaging. This is made possible by various experimental techniques that avoid the time-integration of phase defects introduced by the turbulence. A measure of the quality of the technique is thus the resulting signal-to-noise ratio (SNR) at high spatial frequencies.

10.1.4.1 Speckle techniques

The first high-resolution techniques were based on the acquisition of a series of short-exposure images and the calculation of empirical moments. Speckle interferometry[2] [Lab70] uses the quadratic mean of the FTs of the images, which allows the autocorrelation of the observed object to be estimated. Knox and Thomson [KT74], then Weigelt [Wei77] put forward processing methods using the cross-spectrum and the bi-spectrum respectively of the short-exposure images so as to estimate the object and not only its autocorrelation. These methods require the averages to be taken over a large number of images, even for simple objects, both to make the estimation of the statistical quantities valid and to improve the SNR.

10.1.4.2 Deconvolution from wavefront sensing (DWFS)

A notable enhancement of short-exposure imaging through turbulence was thus brought about, not by improving the processing of measurements but by changing the experimental technique itself. In 1985, Fontanella [Fon85] proposed a new imaging technique: deconvolution from wavefront sensing. This technique, based on the use of a device called a wavefront sensor (WFS), was experimentally validated shortly afterwards [PRF88, PRF90].

The aim of WFSs, which had so far only been used for controlling the surface quality of telescope mirrors, is to measure the aberrations of optical systems (the phase φ

[2]The term interferometry could mislead the reader into thinking that the instrument used here is an interferometer. This is by no means the case; the interferences in question arise from the aperture of a monolithic telescope.

of equation (10.1)). Some of them, such as the Hartmann-Shack sensor used in deconvolution from wavefront sensing, work even if the object of interest is extended (rather than being a point source).

The technique of deconvolution from wavefront sensing consists of simultaneously recording a series of short-exposure images and Hartmann-Shack wavefront measurements. In practice, at least ten or so short-exposure images are typically needed to give correct spatial frequency coverage up to the telescope cut-off (equation (10.6)). The number of images required is greater if the observed object is not very bright.

Deconvolution from wavefront sensing is a considerable improvement on the other short-exposure techniques mentioned above. First of all, like the Knox-Thomson or bi-spectral techniques, it enables us to recover not the autocorrelation of the object but the object itself. Then, unlike the previous short-exposure techniques, this one does not need images of a reference star to be recorded, and it is called *self-referenced speckle interferometry* for this reason. Finally, its measurements are efficient in terms of photons collected: as the short-exposure images must be quasi-monochromatic to keep the speckles unblurred, all the remaining photons can be diverted towards the WFS without any loss of signal on the image channel. This technique thus makes it possible to record more information than the previous short-exposure techniques and, unlike those techniques, has a SNR that is not limited by the speckle noise at high flux [Rod88b], because of its self-referenced nature. This explains why speckle interferometry has fallen into disuse nowadays.

Section 10.4.2 gives more details on the data processing in this technique, which is a double inverse problem (estimation of wavefronts from WFS measurements, which allows the instantaneous PSF corresponding to each image to be calculated, and estimation of the object from images and WFS measurements).

10.1.4.3 Adaptive optics

The imaging technique with the best performance in terms of SNR is adaptive optics (AO), which provides a real-time compensation for the aberrations introduced by atmospheric turbulence, generally by use of a mirror whose surface is deformed at all instants via a servo-loop, according to the measurements made by a WFS.

This technique thus enables long-exposure images (typically exposed for between a few seconds and several tens of minutes) to be recorded while retaining the HFs of the observed object up to the cut-off frequency of the telescope. The HFs are nevertheless attenuated as the correction is only partial [Con94] and deconvolution is necessary. This deconvolution, for which the PSF is often imperfectly known, is presented in section 10.4.3.

The most commonly used WFS is the Hartmann-Shack sensor (see section 10.3.2). The associated deformable mirror has actuators made of, e.g., stacked piezoelectric material controlled by high voltages. The AO technique was proposed by Babcock as early as 1953, and developed from the 1970s for defence purposes, first in the United States, then in France, but it was not until the late 1980s that the first AO system for astronomy came into being [RFK+90]. Any reader interested in a detailed account of AO should consult a reference work such as [Rod99].

10.1.4.4 Optical interferometry

This section describes some of the major steps in the development of ground-based stellar interferometry and takes its inspiration partly from [Mon03].

The first measurements of stars The use of interferometry for observing stars was first suggested by Fizeau in 1868, the aim being simply to measure the size of celestial bodies. However, it was not until 1890 that the technique was implemented experimentally by Michelson [Mic91], who measured the diameters of Jupiter's moons by masking a telescope with two fine slits four inches apart. In 1920-21, he and Pease measured the diameter of the star Betelgeuse using a 20-foot (6-meter) interferometer [MP21].

Pease's unsuccessful attempts to reach a baseline of 50 feet marked the start of a difficult period for optical interferometry. At the same time, the advances made in radar during the Second World War led to the development of interferometry at radio wavelengths. Resolutions smaller than a milliarcsecond were reached in radio interferometry while its optical counterpart rather fell into neglect because of the many technical difficulties involved in coherently combining the beams from two telescopes. In optics, it is impossible to record the phase, and the beams therefore have to be combined in real time. Another handicap for optics is that the effects of turbulence evolve much faster than for radio.

Renewed interest in optical interferometry The first coherent combination of optical beams emitted by a star using a *long baseline* interferometer was achieved by Labeyrie in 1974 [Lab75], with a baseline of 12 meters on a 2-telescope interferometer called I2T. This was followed by a more ambitious version composed of telescopes 1.5 meter in diameter with a baseline of up to 65 meters, which was named the Grand Interféromètre à 2 Téléscopes (GI2T) [MTBB+94]. Up to that time, interferometry had been used with two apertures to measure the spatial spectrum of an astronomical scene from which a few parameters were extracted to validate or reject an astrophysical model. In particular, only the modulus of the spatial spectrum could be used. In addition, without the phase, it is generally impossible to determine the geometry of the observed scene. In 1987, by masking a monolithic telescope, Hannif *et al.* showed that it was possible to obtain interferometric arrays [HMT+87], i.e., to form interference fringes simultaneously for each pair of telescopes of the array. This technique, in addition to providing several measurements at once (15 frequencies per exposure for a 6-telescope interferometer), gave access to the phase of the spatial spectrum of the object [BHMW86], thus making interferometric imaging possible for scenes more complex than a uniform disk or a binary system. The remarkable potential of this method encouraged several teams to build such instruments. In 1995, the COAST interferometer made the first simultaneous combination with three telescopes [BBB+96], and was followed a few months later by NPOI [BHE+97] then IOTA [IOT] (now decommissioned). Since these instruments are evolving quickly, the interested reader is advised to visit `http://olbin.jpl.nasa.gov/` for up-to-date information.

Future of interferometry The technology needed to build optical interferometric arrays has now come of age and draws upon the sister fields of integrated optics, adaptive optics and fiber optics:

- *integrated optics* has been successfully used in multi-telescope simultaneous combination for several years, in particular on the IOTA interferometer [BHK+03] (the experimental data processed at the end of this chapter were obtained with this system);

- *adaptive optics* on large telescopes such as those of the Very Large Telescope Interferometer makes it possible to observe objects of low luminosity;
- *fiber optics* provides monomode fibers that will allow telescopes to be connected interferometrically over very large distances. The OHANA project plans to combine the seven largest telescopes on the summit of Mauna Kea in Hawaii to form an interferometer. The array thus formed will have a maximum baseline of 800 m [PWL+06].

In parallel with the development of these large correlation interferometers, the technology for making *imaging* interferometers is now available. These instruments should eventually lead to considerable savings in volume and mass relative to an equivalent monolithic telescope, which would make them ideal candidates for space missions. On the ground, they would be an alternative to giant monolithic telescopes (of several tens of meters). The first of them is the Large Binocular Telescope LBT [HS04], which will combine two eight-meter telescopes corrected by adaptive optics.

Segmented telescopes, such as those of the Keck Observatory [Kec], have been in use for several years and are at the boundary between imaging interferometers and telescopes. Their primary mirrors are composed of joined petals that are easier to manufacture than a monolithic mirror and this technique has been chosen for the future European giant telescope E-ELT (for *European Extremely Large Telescope*) and the US TMT (for *Thirty Meter Telescope*).

In addition to the correlation and imaging interferometers described in this section, there are other sorts of interferometers. P. Lawson [Law97] has collected together a selection of reference publications in this field as a whole. In this chapter, we shall only deal with the problem of processing the data collected by means of a correlation interferometer observing space from the ground through turbulence.

10.2 Inversion approach and regularization criteria used

Inversion in optical imaging through turbulence is generally an ill-posed problem in the case of a monolithic telescope and an under-determined problem in the case of an interferometer.

In deconvolution from wavefront sensing and in adaptive optics, we need to solve an image restoration problem for which the Bayesian approach already described in this book can be used directly. In the case of so-called *conventional* deconvolution, where the PSF is taken to be perfectly known, the estimated object is defined as the minimizer of a compound criterion containing a data fidelity term J_y and a prior fidelity term J_x. In OI the image is to be reconstructed from heterogeneous data and with a knowledge of the transfer function which is very incomplete because of the turbulence. There are several possible approaches for handling this type of data; the details are given below.

In all cases it is necessary to regularize the inversion to reach acceptable solutions. This will be done here by using a regularization term J_x in the minimized criterion to obtain the solution. The regularization criteria used in this chapter are taken from those described below and are all convex.

Quadratic criteria are the most widely used. We will use a criterion of this type in DWFS and OI with a parametric model of the object spectrum such as the one proposed for adaptive optics in [CMF+98]. An advantage of these criteria is that it is possible to estimate the parameters of the model easily, by maximum likelihood for example. See [BMI03] for the identification of the spectrum model of [CMF+98]

with simultaneous estimation of the aberrations and [GRM+06] for an application to adaptive optics with known PSF. This model can also be identified from the data in OI [Mei05].

For objects with sharp edges such as artificial satellites, asteroids or planets, a quadratic criterion tends to oversmooth the edges and introduce spurious oscillations, or *ringing*, in their neighborhood. A solution is thus to use an edge-preserving criterion such as the so-called quadratic-linear, or L_2L_1, criteria, which are quadratic for weak gradients of the object and linear for the stronger ones. The quadratic part ensures good noise smoothing and the linear part cancels edge penalization (see Chapter 6). Here, for DWFS (section 10.4.2) and AO (section 10.4.3), we will use an isotropic version [MRC+01] of the criterion proposed by Rey [Rey83] in the context of robust estimation and used by Brette and Idier in image restoration [BI96]:

$$J_x(\boldsymbol{x}) = \mu\delta^2 \sum_r \big(\Lambda\boldsymbol{x}(\ell,m)/\delta - \log\left(1+\Lambda\boldsymbol{x}(\ell,m)/\delta\right)\big) \tag{10.8}$$

where $\Lambda\boldsymbol{x}(\ell,m) = \sqrt{\nabla_\xi\,\boldsymbol{x}(\ell,m)^2 + \nabla_\zeta\,\boldsymbol{x}(\ell,m)^2}$, with $\nabla_\xi\,\boldsymbol{x}$ and $\nabla_\zeta\,\boldsymbol{x}$ the gradient approximations by finite differences in the two spatial directions.

For objects composed of bright points on a fairly smooth background, such as are often found in astronomy, we can consider an L_2L_1 prior that is white, i.e., where pixels are independent. Such a prior is obtained by using the regularization of equation (10.8) but with $\Lambda\boldsymbol{x} = \boldsymbol{x}$. This is what we will do for all the interferometric data of section 10.5.4. Unlike for the case of quadratic regularization with an object spectrum model, the tuning of the hyperparameters has to be supervised here.

10.3 Measurement of aberrations

10.3.1 Introduction

The WFS is a key element of modern high-resolution imaging instruments as it allows the instrument aberrations and the atmospheric turbulence to be measured so that they can be compensated for, either in real time (AO) or by post-processing.

Many WFSs are currently available, and a thorough review is given in [Rou99]. They can be divided into two families: focal-plane sensors and pupil-plane sensors.

Present-day AO systems use either a Hartmann-Shack sensor [SP71], which is well described in [Fon85], or a curvature sensor [Rod88a]. Both belong to the pupil-plane family and use a fraction of the incident light, which is diverted by a dichroic beam-splitter. For AO, both have the appealing properties that they work with a broad spectral band (because they can be well described by geometrical optics) and that the relationship between the unknown aberrations and the data is linear, so the inversion can be performed in real time. The next subsection presents the principle of the Hartmann-Shack sensor. This sensor will be seen later in the DWFS technique and is the most widely used in AO.

The focal-plane family of sensors was born from the very natural idea that an image of a given object contains information not only about the object, but also about the wavefront. A focal-plane sensor thus requires little or no optics other than the imaging sensor; it is also the only way to be sensitive to all aberrations down to the focal plane.

Section 10.3.3 briefly presents the focal-plane wavefront sensing technique known as phase diversity [Gon82]. This technique is simple in its hardware requirements and, like the Hartmann-Shack, works on very extended objects. Finally, it should be noted

that there are special WFSs called co-phasing sensors that can measure the differential piston between apertures, which are aberrations specific to interferometers. Phase diversity can be used both as a WFS and as a co-phasing sensor. Differential pistons are not yet corrected on the interferometers in operation at present.

10.3.2 Hartmann-Shack sensor

The principle of this sensor is illustrated in Figure 10.3: an array of $N_{ml} \times N_{ml}$ micro-lenses is placed in a pupil plane (image of the telescope entrance pupil). It samples or, in other words, cuts up the incident wavefront. At the focus of the array, a set of detectors (CCD camera, for example) records the N_{ml}^2 sub-images, each of which is the image of the object observed through the part of the pupil cut out by the corresponding micro-lens. When the wavefront is perturbed by aberrations, each micro-lens sees approximately a tilted plane wavefront and the corresponding sub-image is thus shifted relative to its reference position by an amount proportional to the mean slope of the wavefront. In the case of aberrations due to atmospheric turbulence, N_{ml} should be chosen so that the size of each micro-lens relative to the entrance pupil of the instrument is of the order of the Fried diameter r_0. The position of the center of gravity of each sub-image is measured, thus giving a map of the mean slopes of the wavefront on a $N_{ml} \times N_{ml}$ grid[3].

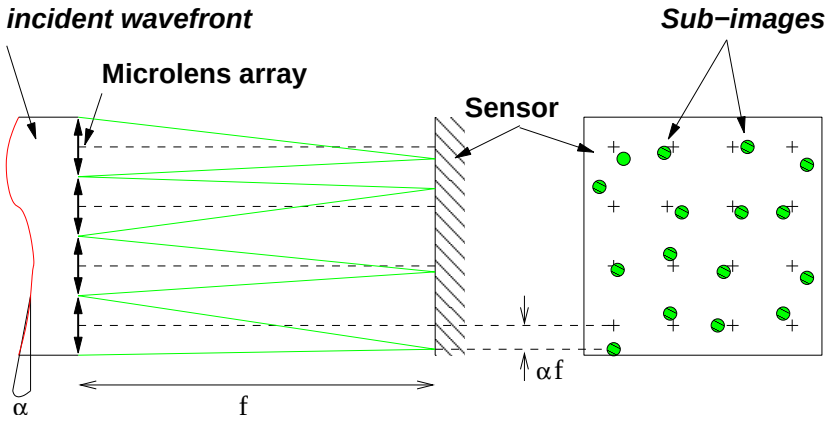

Figure 10.3: Principle of the Hartmann-Shack sensor

The unknown phase at instant t, noted φ_t, is generally expanded into Zernike polynomials [Nol76] and the coefficients of this expansion are noted ϕ_t^q:

$$\varphi_t(\boldsymbol{r}) = \sum_q \phi_t^q Z_q(\boldsymbol{r}) \tag{10.9}$$

where $\boldsymbol{r}$ is the current point in the pupil. The direct problem can then be put in the form:

$$\boldsymbol{s}_t = \mathbf{D}\boldsymbol{\phi}_t + \boldsymbol{b}'_t$$

[3]It is possible to envisage taking the measurements to be not this map of local slopes but directly the set of raw sub-images. In practice, these sub-images generate a large data flow and are therefore not generally stored on a disk: in imaging through turbulence, the wavefront has to be sampled at several tens, or even hundreds, of Hertz.

where $\boldsymbol{s}_t$ is the vector concatenating the $2N_{ml}^2$ slope measurements (x and y), $\boldsymbol{\phi}_t$ is the vector of the coordinates of the unknown phase and $\mathbf{D}$ is essentially a sampled derivation operator called the "interaction matrix".

The noise is generally assumed to be iid Gaussian. The independence among the measurements of the various sub-pupils is natural and the Gaussian character is justified because it results from an estimation of the center of gravity over a "large" number of pixels (typically a few tens).

The solution traditionally used for estimating the phase, in particular under real-time constraints (AO), is the least squares estimation. Matrix $\mathbf{D}^T\mathbf{D}$ is not invertible *a priori* , because the number of measurements is finite ($2N_{ml}^2$), whereas dimension K of vector $\boldsymbol{\phi}$ is, in theory, infinite. In practice, even when K is chosen to be slightly smaller than $2N_{ml}^2$, $\mathbf{D}^T\mathbf{D}$ is ill-conditioned. The usual remedy is to reduce dimension K of the space of unknowns $\boldsymbol{\phi}$ and to filter a few modes that are not seen or are poorly seen by the sensor. These correspond to the few zero or very small eigenvalues of $\mathbf{D}^T\mathbf{D}$. It is common to take $K \simeq N_{ml}^2$.

This remedy works correctly because the Zernike polynomial basis is well suited to atmospheric turbulence. Firstly, these polynomials are in an order corresponding to higher and higher spatial frequencies and the turbulence has a PSD that decreases quite fast (see equation (10.3)), so the diagonal of the turbulent phase covariance matrix on the basis of the Zernikes is decreasing. Secondly, this matrix is concentrated around its diagonal. In other words, the Zernike polynomials Z_i are quite close to the eigen modes (Karhunen-Loève) of the turbulence. In consequence, truncation of the basis $\{Z_i\}$ at a Z_K selects a space containing the most energetic modes. Choosing the best K is quite problematic, as it depends on both the strength of the turbulence r_0 and the noise level on the WFS.

As our statistical knowledge of the turbulence is quite good (see references of section 10.1.3), a Bayesian approach is more appropriate and gives better results.

Since the problem of reconstructing the phase is linear and Gaussian, it leads to an analytical MMSE/MAP estimator, in *covariance* form in [Wal83] and in *information* form in [BKL+94, SM85] (see Chapter 3). MAP estimation of each of the phases corresponds to minimizing the mixed criterion $J_{\text{MAP}}^{\phi} = J_s + J_\phi$, with:

$$J_s = \frac{1}{2}(\boldsymbol{s}_t - \mathbf{D}\boldsymbol{\phi}_t)^T \mathbf{C}_{b'}^{-1}(\boldsymbol{s}_t - \mathbf{D}\boldsymbol{\phi}_t) \tag{10.10}$$

and

$$J_\phi = \frac{1}{2}\boldsymbol{\phi}_t^T \mathbf{C}_\phi^{-1}\boldsymbol{\phi}_t \tag{10.11}$$

where $\mathbf{C}_{b'}$ is the covariance matrix of the slope measurement noise (diagonal, with a practically constant diagonal) and $\mathbf{C}_\phi$ is the covariance matrix of the turbulent phase in the Zernike basis, which is deduced from equation (10.3) [Nol76] depending only on r_0. The well known solution is:

$$\widehat{\boldsymbol{\phi}}_t = (\mathbf{D}^T\mathbf{C}_{b'}^{-1}\mathbf{D} + \mathbf{C}_\phi^{-1})^{-1}\mathbf{D}^T\mathbf{C}_{b'}^{-1}\boldsymbol{s}_t. \tag{10.12}$$

This solution takes advantage of our knowledge of the spatial statistics of the turbulence. For use in AO, where the sampling frequency is generally well above $1/\tau_0$, it is judicious to opt for a natural extension of this MMSE estimator that also uses prior knowledge on the time statistics of the turbulence. This extension is the optimal estimator of Kalman filtering [LRCK+04, PCK+05, KRP+06].

10.3.3 Phase retrieval and phase diversity

Phase retrieval consists of estimating the aberrations seen by an instrument from the image of a point source. This comes down to inverting equation (10.1), i.e., estimating its phase φ from a measurement of h. This technique, first used in electron microscopy [GS72a] then rediscovered in optics [Gon76], has two main limitations: (i) it only works with a point object and (ii) the solution obtained suffers from sign ambiguity and is generally not unique.

Gonsalves [Gon82] has shown that, by using a second image containing a known variation in the aberrations with respect to the first, e.g. a slight defocus, it is possible to estimate the aberrations even if the object is spatially extended and unknown. Moreover, this second image lifts the indetermination mentioned above and the estimated aberrations are unique, in practice, for small aberrations. This technique is called phase diversity by analogy with a technique used in wireless telecommunications.

Phase diversity is used in two different contexts. We may wish to obtain an image of a remote object, e.g. in solar astronomy, or we may wish to measure the aberrations seen by an instrument in order to correct them in real time or off-line. These two problems are connected but nevertheless distinct. In both cases, the basis of the inversion is to estimate the aberrations and object that are the most compatible with the measured images. The conventional approach is a joint estimation of the object and the phase [Gon82] possibly with a regularization for both unknowns. Although this type of joint estimation usually has poor statistical properties, in the specific case of phase diversity, it has been shown that joint estimation leads to a consistent estimator for aberrations [IMB05]. In addition, a so-called marginal approach that integrates the object out of the problem so as to only estimate the phase has been proposed recently and leads to better robustness with respect to noise [BMI03].

The interested reader will find a more complete history and a review of the applications of this WFS in [MBI06], which also contains a detailed study of the two estimators mentioned above.

10.4 Myopic restoration in imaging

10.4.1 Motivation and noise statistic

In imaging through turbulence with a monolithic telescope, the data processing needed is essentially a deconvolution. Nevertheless, the estimation or the measurement of the PSF is often imperfect and the best deconvolution results are generally obtained by specifically taking the partial lack of knowledge of the instrument's response into account. This is what we will call myopic deconvolution, which can take different forms depending on whether the turbulence is corrected off line, by DWFS (section 10.4.2) or in real time by AO (section 10.4.3).

The most used data-fidelity term is the ordinary least squares criterion. In a probabilistic interpretation, this criterion corresponds to the assumption that the noise is white, Gaussian and stationary (see Chapter 3):

$$J_y(\boldsymbol{x}) = \frac{1}{2\sigma_b^2} \|\mathbf{H}\boldsymbol{x} - \boldsymbol{y}\|^2 \tag{10.13}$$

where $\boldsymbol{x}$ is the observed object, $\boldsymbol{y}$ the recorded image, $\mathbf{H}$ the imaging operator and σ_b the standard deviation of the noise. In astronomical imaging, this interpretation is

generally a crude approximation, except for a large bright object, as the predominant noise is generally photonic and thus follows Poisson statistics leading to the following data-fidelity term:

$$J_y(\boldsymbol{x}) = \sum_{\ell,m} (\mathbf{H}\boldsymbol{x} - \boldsymbol{y} \log \mathbf{H}\boldsymbol{x})(\ell, m) \tag{10.14}$$

This non-quadratic criterion can cause practical difficulties for the minimization when gradient-based numerical methods are used. What is more, in very dark parts of the image, the electronic noises of the sensor become non-negligible relative to the photonic noise and fine modeling of the noise must take the simultaneous presence of noise from the sensor (typically a CCD device) and photonic noise into account. These specific difficulties will be examined more closely in Chapter 14.

A good compromise between fine modeling of the noise and efficient minimization can be obtained as follows. A quadratic approximation of (10.14) is deduced first, which corresponds to purely photonic noise. For an image that is not too dark (in practice, ten or so photons per pixel can suffice), the approximation $\mathbf{H}\boldsymbol{x} - \boldsymbol{y} \ll \boldsymbol{y}$ can be taken and (10.14) expanded to the second order. The result corresponds to white, non-stationary, Gaussian noise with variance equal to the image at each point. Then, by simply summing the variances, a data-fidelity criterion is obtained that models the simultaneous presence of sensor and photonic noise [MFC04]:

$$J_y(\boldsymbol{x}) = \sum_{\ell,m} \frac{1}{2(\sigma^2_{\text{ph}}(\ell, m) + \sigma^2_{\text{det}})} |(\mathbf{H}\boldsymbol{x})(\ell, m) - \boldsymbol{y}(\ell, m)|^2 \tag{10.15}$$

where $\sigma^2_{ph}(\ell, m) = \max\{\boldsymbol{y}(\ell, m), 0\}$ is an estimator of the variance of the photonic noise at each pixel and σ^2_{det} the variance of the sensor noise, estimated beforehand.

10.4.2 Data processing in deconvolution from wavefront sensing

10.4.2.1 Conventional processing of short-exposure images

In this subsection, we describe non-myopic multiframe deconvolution; in other words, we consider that the PSFs deduced from the WFS measurements are true. In the next subsection, we show how a myopic deconvolution, i.e., the joint processing of WFS data and images, can improve the estimation of the observed object.

We have a series of N_{im} short-exposure images of an object that is smaller than the isoplanatic patch. The equation of the discretized direct problem can be written:

$$\boldsymbol{y}_t = \boldsymbol{h}_t \star \boldsymbol{x} + \boldsymbol{b}_t = \mathbf{H}_t \boldsymbol{x} + \boldsymbol{b}_t, \quad 1 \leq t \leq N_{im} \tag{10.16}$$

where $\boldsymbol{x}$ and $\boldsymbol{y}_t$ are the discretized object and image respectively at time t and where the PSF $\boldsymbol{h}_t$ is related to the phase φ_t in the pupil at the same instant by Equation (10.1). We also have wavefront measurements, in this case Hartmann-Shack slope measurements $\boldsymbol{s}_t$ associated with each image.

The conventional DWFS data processing is sequential: first we estimate the phases $\boldsymbol{\phi}_t$ via (10.12), then deduce the PSFs $\boldsymbol{h}_t$ via (10.1) and finally estimate the object by multiframe deconvolution. The details of this sequential processing are given below.

The image processing used in the early days of the DWFS technique was a simple multiframe least squares [PRF90]; the solution was thus the multiframe inverse filter, which in practice had to be regularized by adding a small constant to the denominator in the Fourier domain. A better approach is to explicitly regularize the criterion to

be minimized. For objects with clearly marked edges such as artificial satellites, the regularization criterion to be used is the L_2L_1 of equation (10.8).

Using the Bayesian framework presented in Chapter 3, we estimate the object in the MAP sense. Two considerations allow the likelihood of the set of images to be simplified: firstly, the noise is independent between images and, secondly, the delay between successive acquisitions is generally longer than the typical turbulence evolution time. The likelihood can thus be rewritten as the product of the likelihoods of the individual images, each being conditioned simply by the object and the phase at the same instant. The estimate of the object is then the one that minimizes

$$J^x_{\text{MAP}}(\boldsymbol{x}) = \sum_{t=1}^{N_{\text{im}}} J_y(\boldsymbol{x}; \boldsymbol{\phi}_t, \boldsymbol{y}_t) + J_x(\boldsymbol{x}), \tag{10.17}$$

where $J_y(\boldsymbol{x}; \boldsymbol{\phi}_t, \boldsymbol{y}_t) = -\log p(\boldsymbol{y}_t \,|\, \boldsymbol{x}, \boldsymbol{\phi}_t)$. In practice, for both simulations (see section 10.4.2.3) and experimental data (see section 10.4.2.4), the data-fidelity term used for J_y will be the least squares term of equation (10.13). The minimization is performed numerically on the object variables and the presence of the $\boldsymbol{\phi}_t$ in the J^x_{MAP} criterion above is simply a reminder of the dependence of the criterion on the phase.

10.4.2.2 Myopic deconvolution of short-exposure images

In conventional DWFS data processing, the information concerning the wavefronts is extracted from the WFS data only, not from the images. And yet there is exploitable information on the PSF in the short-exposure images, as proved by the results some authors [Sch93, TC95] have obtained by blind deconvolution (i.e., without WFS, but using the models (10.1) and (10.9)).

However, the criteria to be minimized in blind deconvolution generally have local minima and parametrizing the PSF by the pupil phase is not sufficient to ensure that the solution is unique. This is why WFS data should certainly not be ignored but should rather be used in conjunction with the images.

Myopic deconvolution consists of searching for the most probable object $\boldsymbol{x}$ and turbulent phases $\boldsymbol{\phi}_t$ jointly, given the images $\boldsymbol{y}_t$, the WFS measurements $\boldsymbol{s}_t$ and the prior information on $\boldsymbol{x}$ and $\boldsymbol{\phi}_t$ [MRC+01]. Using Bayes' rule and the same independence hypotheses as in section 10.4.2.1, it can be shown that the estimates $(\widehat{\boldsymbol{x}}, \{\widehat{\boldsymbol{\phi}}_t\})$ in the joint MAP sense are those that minimize:

$$J_{\text{MAP}}(\boldsymbol{x}, \{\boldsymbol{\phi}_t\}) = \sum_{t=1}^{N_{\text{im}}} J_y(\boldsymbol{x}, \boldsymbol{\phi}_t\,;\, \boldsymbol{y}_t) + J_x(\boldsymbol{x}) + \sum_{t=1}^{N_{\text{im}}} J_s(\boldsymbol{\phi}_t\,;\, \boldsymbol{s}_t) + \sum_{t=1}^{N_{\text{im}}} J_\phi(\boldsymbol{\phi}_t)$$

where:

- the J_y are the image-fidelity terms; $J_y(\boldsymbol{x}, \boldsymbol{\phi}_t; \boldsymbol{y}_t)$ is the anti-log-likelihood of the tth image; it is now a function of the object *and* the phases;
- $J_x(\boldsymbol{x})$ is the object prior, which, in what follows, will be the L_2L_1 model of equation (10.8);
- the J_s are the fidelity to WFS data terms; with the hypotheses used, they are quadratic and given by equation (10.10);
- the J_ϕ are the *a priori* terms on the phases given by equation (10.11).

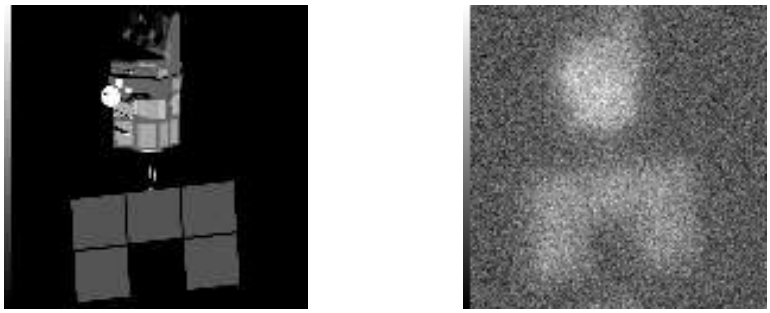

Figure 10.4: Original object (SPOT satellite, left) and one of the 100 short-exposure images ($D/r_0 = 10$, right)

The criterion is minimized by a method based on conjugate gradients, alternating minimizations on the object $\boldsymbol{x}$ (for the current phase estimate) and on the set of phases $\boldsymbol{\phi}_t$ (for the current object estimate).

To speed up the minimization and also to avoid, in practice, the local minima often present in joint criteria, the initial object and phases are taken to be the MAP estimates obtained in the sequential processing described in section 10.4.2.1.

10.4.2.3 Simulations

A set of 100 images were simulated with the associated WFS measurements. The 100 wavefronts were obtained by a modal method [Rod90] in which each phase is expanded on a basis of Zernike polynomials (see equation (10.9)) and follows Kolmogorov statistics (see equation (10.3)). The turbulence strength corresponds to a ratio $D/r_0 = 10$. Each of the turbulent wavefronts is used to calculate a short-exposure image of dimensions 128×128, sampled at the Shannon frequency using equations (10.1) and (10.16). The noise added to the images is white, Gaussian and stationary with a variance equal to the mean flux to be simulated, i.e., $10^4/128^2 = 0.61$ photon/pixel. Figure 10.4 shows the object, which is a numerical model of the SPOT satellite, and one of the 100 simulated images. The corresponding PSF is the image on the left of Figure 10.2. The simulated WFS is a Hartmann-Shack having 20×20 sub-apertures, without central obscuration. White Gaussian noise is added to the local slopes of the wavefront so that the SNR of the slopes measured, defined as the variance of the slopes over the variance of the noise, is 1.

Figure 10.5 compares the results of the sequential and myopic estimations for the same L_2L_1 prior on the object (equation (10.8)), associated with a positivity constraint[4]. On the left, the non-myopic restoration is the MAP estimation of the wavefronts followed by a restoration with PSFs deduced from the estimated wavefronts and gives an MSE with the actual object of 0.45 photon (per pixel). On the right, the joint estimation gives an MSE of 0.39 photon. In addition, the myopic estimation also allows the quality of the reconstructed wavefronts to be improved [MRC+01].

[4] Our thanks to Clélia Robert for processing the DWFS data.

Figure 10.5: Object restored by non-myopic (left) and myopic (right) estimation. In both cases, an L_2L_1 prior and an object positivity constraint were used. The MSE with the actual object are 0.45 and 0.39 photon respectively

10.4.2.4 Experimental results

The processing methods described above were applied to ten experimental images of the double star Capella recorded on 8th November 1990 with the DWFS system of ONERA, installed on the 4.20-meter-diameter William Herschel telescope (La Palma, Canary Islands). The experimental conditions were the following: a flux of $67,500$ photons per image, an exposure time of 5 ms, a D/r_0 of 13 and a SNR of 5 on the WFS. The WFS was a Hartmann-Shack with 29×29 sub-apertures, 560 of which were used.

Figure 10.6, taken from [MRC+01], shows the results of the deconvolution. On the left, the sequential processing consisted of an estimation of the wavefronts by MAP, then a quadratic image restoration. The binary nature of Capella is visible, but is almost drowned in strong fluctuations. On the right, the myopic deconvolution has eliminated almost all the artefacts of the non-myopic deconvolution. In both cases, the same quadratic object regularization with a positivity constraint was used, with a constant PSD whose value was deduced from the measured flux.

Figure 10.6: Deconvolved experimental images of Capella: left, estimation of wavefronts by MAP then quadratic deconvolution; right, myopic deconvolution. In both cases, the prior used was Gaussian with a constant PSD deduced from the measured flux, with a positivity constraint

10.4.3 Restoration of images corrected by adaptive optics

10.4.3.1 Myopic deconvolution of images corrected by adaptive optics

Long-exposure images corrected by AO must be deconvolved, since the correction is only partial [Con94]. If we take the PSF as known, the object estimated in the MAP sense, noted $\widehat{\boldsymbol{x}}_{\text{MAP}}$, is the one that maximizes $p(\boldsymbol{x} \,|\, \boldsymbol{y}\,;\, \boldsymbol{h})$, and thus minimizes $J_y(\boldsymbol{x}\,;\, \boldsymbol{h}, \boldsymbol{y}) + J_x(\boldsymbol{x})$. The most usual method for estimating the PSF is to record the image of a star just before or just after the image of the object of interest. This star image may be noticeably different from the PSF corresponding to the image we are interested in for a variety of reasons: first, the turbulence changes with time [CFM+98]; thus, the response of the AO may be different when going from a spatially extended object to a point object, even if the star is of the same magnitude as the object, since the wavefront sensing error increases with the extent of the object; and finally, there is noise on the star image itself. A method has been proposed and validated for estimating the turbulent part of the long-exposure transfer function corrected by the AO from measurements of the residual wavefront of the control loop [Ver97, VRMR97]. Nevertheless, apart from the fact that the static or slowly varying aberrations of the telescope may not be properly known, the accuracy of this estimation of the transfer function is limited by the noise on the WFS. Thus, it is often necessary to consider that the PSF is imperfectly known.

Many authors have tackled the problem of deconvolving an image degraded by turbulence with unknown PSF. Ayers and Dainty [AD88] used a Gerchberg-Saxton-Papoulis algorithm [GS72b] and came up against problems of convergence with this type of algorithm. Others have used maximum likelihood methods, with an EM algorithm [Hol92] or minimization of an explicit criterion [JC93, Lan92, Lan96, TC95]. They generally recognize the need for regularization other than just positivity (of the object and the PSF) and, in particular, have introduced a (legitimate) limited bandwidth constraint on the PSF through an ad hoc prior [Hol92, JC93].

The Bayesian framework allows this joint estimation (called myopic estimation) of the object and the PSF to be made with a natural regularization for the PSF and without having to adjust any additional hyperparameters. The joint MAP estimator is given by:

$$\begin{aligned}(\widehat{\boldsymbol{x}}, \widehat{\boldsymbol{h}}) &= \arg\max_{\boldsymbol{x},\boldsymbol{h}} p(\boldsymbol{x}, \boldsymbol{h}|\boldsymbol{y}) = \arg\max_{\boldsymbol{x},\boldsymbol{h}} p(\boldsymbol{y}|\boldsymbol{x}, \boldsymbol{h}) \times p(\boldsymbol{x}) \times p(\boldsymbol{h}) \\ &= \arg\min_{\boldsymbol{x},\boldsymbol{h}} \left(J_y(\boldsymbol{x}, \boldsymbol{h}; \boldsymbol{y}) + J_x(\boldsymbol{x}) + J_h(\boldsymbol{h})\right)\end{aligned}$$

The long-exposure PSF can be considered as the sum of a large number of independent short-exposure PSFs, and thus modeled by a Gaussian prior (truncated to positive values). We also assume that the difference between the PSF and the mean PSF is approximately stationary. The regularization of the PSF is thus a quadratic penalization of the transfer function, which is independent between frequencies [CMF+98, FVCM99, MFC04]:

$$J_h(\boldsymbol{h}) = \frac{1}{2} \sum_f |\widehat{\boldsymbol{h}}(\boldsymbol{u}) - \widehat{\boldsymbol{h}}_m(\boldsymbol{u})|^2 / S_h(\boldsymbol{u})$$

where $\widehat{\boldsymbol{h}}_m = \mathrm{E}(\widehat{\boldsymbol{h}})$ is the mean transfer function and $S_h = \mathrm{E}(|\widehat{\boldsymbol{h}}(\boldsymbol{u}) - \widehat{\boldsymbol{h}}_m(\boldsymbol{u})|^2)$ the energy spectral density (ESD) of the PSF. Note that S_h is zero beyond the cut-off frequency of the telescope and that this regularization, in particular, forces $\boldsymbol{h}$ to comply with the limited bandwidth constraint.

In practice, the mean transfer function and the ESD of the PSF are estimated by replacing the expectations in their definitions by empirical means on the various images of the star acquired before or after the object of interest. If only a single image of the star is available, the expectation can be replaced by a circular mean in the Fourier domain because of the isotropy of the quantities to be estimated.

In order to be able to restore objects with a large dynamic range, which are frequent in astronomy, the data-fidelity term J_y must include fine modeling of the noise, such as the mixture of photonic and electronic noise of equation (10.15), rather than a simple least squares. The regularization criterion J_x used here is the L_2L_1 model of equation (10.8), which is well suited to objects with sharp edges such as planets and asteroids.

The restoration method known as MISTRAL [MFC04] combines the myopic estimation of the object and PSF described earlier with the white inhomogenous data-fidelity term and the L_2L_1 regularization just mentioned. This method was used to obtain the deconvolution results presented below. The criterion was minimized by the conjugate gradient method, jointly on the object and PSF variables. A positivity constraint was added on $\boldsymbol{x}$ and on $\boldsymbol{h}$.

10.4.3.2 Experimental results

Figure 10.7(a) shows an AO-corrected long-exposure image of Ganymede, a satellite of Jupiter. This image was recorded on 28th September 1997 on the ONERA AO system installed on the 1.52 m telescope of the Haute-Provence observatory. This system has an 80 Hz passband; it comprises a Hartmann-Shack wavefront sensor with 9×9 sub-apertures (64 of which are active) and a deformable mirror with 10×10 piezo actuators, 88 of which are active. The imaging wavelength is $\lambda = 0.85\,\mu$m and the exposure time 100 s. The total estimated flux is 8.10^7 photons and the estimated D/r_x ratio is 23. The total field is 7.9 arcsec, only half of which is shown here. The mean PSF and its ESD were estimated from fifty recorded images of a nearby bright star. Figures 10.7(b) and c show the restorations obtained by the Richardson-Lucy algorithm (maximum likelihood for a Poisson noise), interrupted at 200 and $3{,}000$ iterations respectively. In the first case, the restored image is quite blurred and shows ringing, and in the second case, the noise dominates the restoration. The image of Figure 10.8(a) illustrates myopic deconvolution [MFC04] with an L_2L_1prior[5]. Figure 10.8(b) shows a wideband synthetic image obtained from photos taken by a NASA/JPL space probe (see `http://space.jpl.nasa.gov/`) as it passed near Ganymede. The comparison shows that many features of Ganymede have been correctly restored. A fairer comparison is to examine the myopic deconvolution performed by MISTRAL together with the image of Figure 10.8(b) convolved with the perfect PSF of a 1.52 m telescope, presented in Figure 10.8(c).

Figure 10.9 shows three images of Neptune recorded at half-hour intervals on 6th July 1998 with the curvature-based adaptive optics system of the Institute for Astronomy of the University of Hawaii[6] called Hokupa'a. This system, which was in operation until 2003, had thirty-six actuators and was installed on the Canada-France-Hawaii (CFH) 3.6 m telescope. It produced the first high-resolution infra-red images of Neptune in November 1997 and July 1998 [RRG+98]. The imaging wavelength was $1.72\,\mu$m, which is situated in a methane absorption band. The exposure time was 10 minutes per image. The images restored by myopic deconvolution with an prior

[5] Our thanks to Thierry Fusco for processing the AO images.

[6] Our thanks to François and Claude Roddier for so kindly providing us with these images.

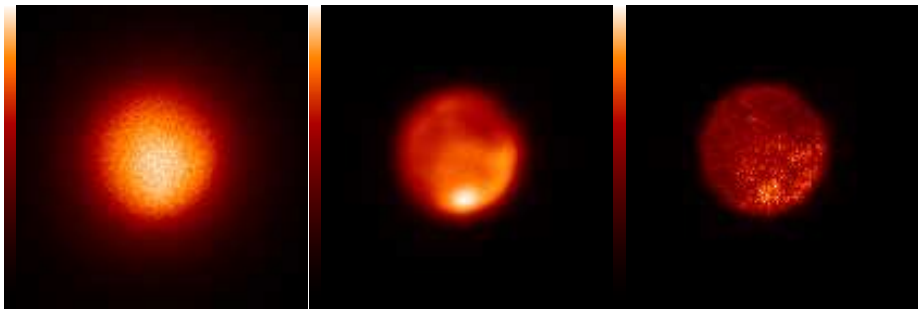

(a) image corrected by AO (b) Richardson-Lucy, 200 it. (c) Richardson-Lucy, $3{,}000$ it.

Figure 10.7: (a) Observation of Ganymede with the ONERA AO system on 28th September 1997. (b) Richardson-Lucy restoration interrupted at 200 iterations; (c) idem at $3{,}000$ iterations

(a) L_2L_1 myopic deconvolution (b) JPL database (NASA/JPL/Caltech) (c) image (b) + PSF of perfect telescope

Figure 10.8: (a) L_2L_1 myopic deconvolution of the image of Ganymede of Figure 10.7. (b) For comparison, a wideband synthetic image obtained from the NASA/JPL database. (c) Same synthetic image convolved by the perfect PSF of a 1.52 m-diameter telescope

are shown in Figure 10.10 [CFM+00]. The image of a star near Neptune was also recorded in order to estimate the mean PSF and the ESD of the PSF by the circular mean in the Fourier domain. Because the atmosphere of Neptune is very dark at the imaging wavelength, these images show the fine structures of the cloud bands in the upper atmosphere with good contrast. Note, in particular, that the fine structures of the cloud bands can be followed from image to image as the planet turns. This was the first time it had been possible to study the details of Neptune's atmospheric activity from the ground.

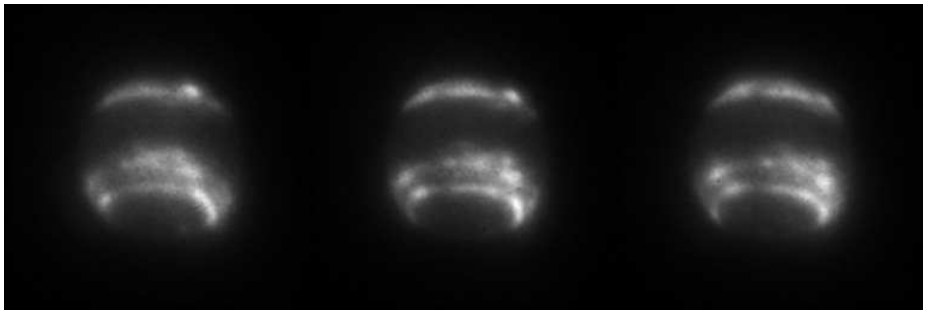

Figure 10.9: Images of Neptune obtained at 30-minute intervals on 6th July 1998 with the Hokupa'a adaptive optics system on the Canada-France-Hawaii telescope. The imaging wavelength was $1.72\ \mu$m and the exposure time for each image was 10 minutes

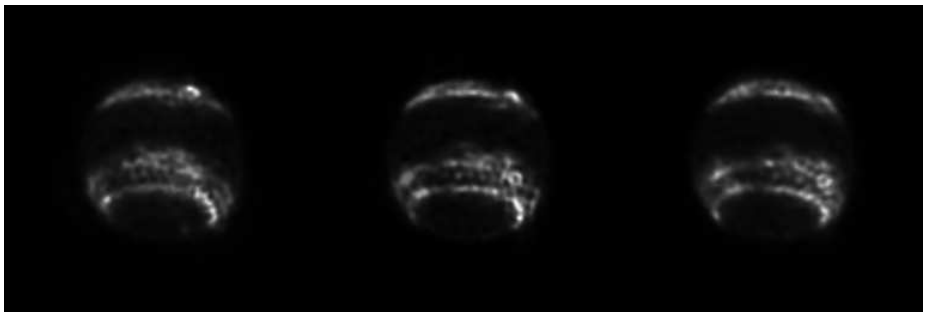

Figure 10.10: Images of Figure 10.9 restored by myopic deconvolution with L_2L_1 prior

10.4.4 Conclusion

The restoration of images degraded by turbulence and corresponding to a convolutive imaging model is now a well mastered technique. The observation systems currently being developed have more complex acquisition modes for which processing will no doubt be largely called upon. Representative examples are the wide-field systems with so-called multiconjugate AO [CR05], for which the PSF cannot be considered as spatially invariant, and the systems such as SPHERE [DBF+06] or GPI that combine high-performance AO (known as extreme AO) with a coronograph in the aim of detecting exoplanets. For such systems, imaging is fundamentally non-convolutive and specific processing has to be developed. AO has also found an application in retinal imaging

in recent years and several teams are developing operational systems (see for example [Gla02, GGL+04] and the references therein). In this context, the image measured and the object to be restored are three-dimensional [CMLG07].

10.5 Image reconstruction in optical interferometry (OI)

This section is devoted to the reconstruction of images from data coming from a correlation interferometer. Section 10.1.2.2 presented the measurement principle and the type of transfer function associated with these systems. The observation model is presented more precisely in section 10.5.1, then sections 10.5.2 and 10.5.3 describe the main avenues towards image reconstruction at present. Finally, results on synthetic and real data are the subject of section 10.5.4.

10.5.1 Observation model

Let us consider a two-telescope interferometer. The positions of the telescopes in a plane normal to the observation direction are $\boldsymbol{r}_1$ and $\boldsymbol{r}_2$. Due to the Earth's rotation, the observation direction changes with time and the baseline $\boldsymbol{r}_2 - \boldsymbol{r}_1$ thus varies, as does the spatial frequency corresponding to it:

$$\boldsymbol{u}_{12}(t) \triangleq (\boldsymbol{r}_2(t) - \boldsymbol{r}_1(t))/\lambda.$$

When a *complete* interferometer array is used, i.e., one in which all the possible two-telescope baselines can be formed simultaneously, there are $N_b = N_t(N_t-1)/2$ measurement frequencies given by

$$\boldsymbol{u}_{k\ell}(t) = (\boldsymbol{r}_\ell(t) - \boldsymbol{r}_k(t))/\lambda, \quad 1 \leq k < \ell \leq N_t.$$

Each baseline (T_k, T_ℓ) produces interference fringes. The measurement of the contrast and position of these fringes defines the complex visibility $y_{k\ell}^{\text{data}}(t)$ and gives information on the modulus $a_{k\ell}(\boldsymbol{x}, t)$ and the phase $\phi_{k\ell}(\boldsymbol{x}, t)$ of the FT of object $\boldsymbol{x}$ at spatial frequency $\boldsymbol{u}_{k\ell}$.

When the instrument is calibrated, generally by prior observation of an unresolved object, we no longer have to consider the possibly complex gains, that come into measurement (10.7) presented in section 10.1.2.2. On the other hand, the effects of turbulence, which vary rapidly, cannot be precalibrated. We can thus take it that the main perturbation affecting the *short-exposure* phase measurement is an additive term $\varphi_\ell(t) - \varphi_k(t)$ known as the differential piston term:

$$\phi_{k\ell}^{\text{data}}(t) = \phi_{k\ell}(\boldsymbol{x}, t) + \varphi_\ell(t) - \varphi_k(t) + \text{noise } [2\pi] \tag{10.18}$$

where $\phi_{k\ell}^{\text{data}}(t)$ is the phase of $y_{k\ell}^{\text{data}}(t)$. Thus, in matrix form, $\boldsymbol{\phi}^{\text{data}}(t) = \boldsymbol{\phi}(\boldsymbol{x}, t) + \boldsymbol{B}\boldsymbol{\varphi}(t) + \text{noise } [2\pi]$, where the *baseline operator* $\boldsymbol{B}$ has dimensions $N_b \times N_t$.

As mentioned in section 10.1.2.2, the differential piston is the result of the random differences introduced in the optical path between the apertures of the system by turbulence. For a long baseline (relative to the Fried diameter), the optical path difference may be very much greater than the observation wavelength and thus lead to random phase differences much larger than 2π. The aliased perturbation that affects the phase (10.18) is then practically uniformly distributed in $[0, 2\pi]$. In consequence, averaging

the phases of short-exposure visibility (10.18) does not improve the signal-to-noise ratio. A solution is to carry out *phase closures* [Jen58] before the averaging. For any set of three telescopes (T_k, T_ℓ, T_m) the short-exposure visibility phase data is

$$\begin{cases} \phi_{k\ell}^{\text{data}}(t) = \phi_{k\ell}(\boldsymbol{x}, t) + \varphi_\ell(t) - \varphi_k(t) + \text{noise} \\ \phi_{\ell m}^{\text{data}}(t) = \phi_{\ell m}(\boldsymbol{x}, t) + \varphi_m(t) - \varphi_\ell(t) + \text{noise} \\ \phi_{mk}^{\text{data}}(t) = \phi_{mk}(\boldsymbol{x}, t) + \varphi_k(t) - \varphi_m(t) + \text{noise} \end{cases} \tag{10.19}$$

and the turbulent pistons are canceled out in the closure phase defined by:

$$\begin{aligned} \beta_{k\ell m}^{\text{data}}(t) &\triangleq \phi_{k\ell}^{\text{data}}(t) + \phi_{\ell m}^{\text{data}}(t) + \phi_{mk}^{\text{data}}(t) + \text{noise} \\ &= \phi_{k\ell}(\boldsymbol{x}, t) - \phi_{\ell m}(\boldsymbol{x}, t) + \phi_{mk}(\boldsymbol{x}, t) + \text{noise} \\ &= \beta_{k\ell m}(\boldsymbol{x}, t) + \text{noise} \end{aligned} \tag{10.20}$$

To form this type of expression it is necessary to measure 3 visibility phases simultaneously, and thus to use an array of 3 telescopes or more. For a complete array made up of N_t telescopes, the set of closure phases that can be formed is generated by, for example, the $\beta_{1k\ell}^{\text{data}}(t)$, $1 < k < \ell \leq N_t$, i.e., the closure phases measured on the triangles of telescopes including T_1. It is easy to see that there are $(N_t - 1)(N_t - 2)/2$ of these independent closure phases. In what follows, the vector grouping together these independent closure phases will be noted $\boldsymbol{\beta}^{\text{data}}$ and a closure operator $\boldsymbol{C}$ is defined such that

$$\boldsymbol{\beta}^{\text{data}} \triangleq \boldsymbol{C}\boldsymbol{\phi}^{\text{data}} = \boldsymbol{C}\boldsymbol{\phi}(\boldsymbol{x}, t) + \text{noise}.$$

The second equation is a matrix version of (10.20): the closure operator cancels the differential pistons, a property that can be written $\boldsymbol{C}\boldsymbol{B} = \boldsymbol{0}$. It can be shown that this equation implies that the closure operator has a kernel of dimension $N_t - 1$, given by

$$\text{Ker}\, \boldsymbol{C} = \left\{ \bar{\boldsymbol{B}}\boldsymbol{\alpha}, \boldsymbol{\alpha} \in \mathbb{R}^{N_t - 1} \right\} \tag{10.21}$$

where $\bar{\boldsymbol{B}}$ is obtained by removing the first column from $\boldsymbol{B}$. The closure phase measurement thus does not allow all the phase information to be measured. This result can also be obtained by counting up the phase unknowns, i.e., $N_t(N_t - 1)/2$ object visibility phases minus the number of independent closures, $(N_t - 1)(N_t - 2)/2$, which gives $N_t - 1$ missing phase data. In other words, optical interferometry through turbulence comes under Fourier synthesis *with partial phase information*. Note that, the more apertures there are in the array, the smaller the proportion missing information will be.

We are now in a position to define the long-exposure observables of a correlation interferometer:

- *mean square amplitudes* $\boldsymbol{s}^{\text{data}}(t) = \left\langle (\boldsymbol{a}^{\text{data}}(t + \tau))^2 \right\rangle_\tau$, in preference to mean moduli as they have an easy-to-calculate bias, which can be subtracted from the measurements
- *bispectra* $V_{1k\ell}^{\text{data}}(t)$, $k < \ell$, defined by

$$V_{1k\ell}^{\text{data}}(t) = \left\langle y_{1k}^{\text{data}}(t + \tau) y_{k\ell}^{\text{data}}(t + \tau) y_{l1}^{\text{data}}(t + \tau) \right\rangle_\tau.$$

The modulus of the bispectrum is redundant with the squares of the amplitudes and is thus not used in image reconstruction. The phases of the bispectra $\beta_{1k\ell}^{\text{data}}(t)$, $k < \ell$ constitute unbiased long-exposure closure phase estimators.

Notation τ expresses the averaging in a time interval around instant t, an interval that must be short enough for the spatial frequency to be considered constant during the integration despite the rotation of the Earth. The integration time also determines the standard deviations of the residual noises on the measurements.

The long-exposure observation model is finally:

$$\begin{cases} \boldsymbol{s}^{\text{data}}(t) = \boldsymbol{a}^2(\boldsymbol{x},t) + \boldsymbol{s}^{\text{noise}}(t), & \boldsymbol{s}^{\text{noise}}(t) \sim \mathcal{N}\left(0, \boldsymbol{R}_{\boldsymbol{s}(t)}\right) \\ \boldsymbol{\beta}^{\text{data}}(t) = \boldsymbol{C}\boldsymbol{\phi}(\boldsymbol{x},t) + \boldsymbol{\beta}^{\text{noise}}(t), & \boldsymbol{\beta}^{\text{noise}}(t) \sim \mathcal{N}\left(0, \boldsymbol{R}_{\boldsymbol{\beta}(t)}\right) \end{cases} \tag{10.22}$$

Estimating an object from such Fourier data is called *Fourier synthesis*. Matrices $\boldsymbol{R}_{\boldsymbol{s}(t)}$ and $\boldsymbol{R}_{\boldsymbol{\beta}(t)}$ are generally assumed to be diagonal. In terms of prior knowledge, the object we are looking for is positive. Moreover, as visibilities as flux-normalized quantities, it is convenient to work with the constraint of unit flux. The constraints on the object are thus

$$\begin{aligned} \sum_{k,\ell} x(k,\ell) &= 1 \\ \forall k,\ell,\ x(k,\ell) &\geq 0 \end{aligned} \tag{10.23}$$

10.5.2 Traditional Bayesian approach

This approach first forms the anti-log-likelihood according to model (10.22)

$$J^{\text{data}}(\boldsymbol{x}) = \sum_t J^{\text{data}}(\boldsymbol{x},t) = \sum_t \chi^2_{\boldsymbol{s}(t)}(\boldsymbol{x}) + \chi^2_{\boldsymbol{\beta}(t)}(\boldsymbol{x}) \tag{10.24}$$

with the notation

$$\chi^2_{\boldsymbol{m}(t)}(\boldsymbol{x}) \triangleq \left(\boldsymbol{m}^{\text{data}}(t) - \boldsymbol{m}(\boldsymbol{x},t)\right)^T \boldsymbol{R}^{-1}_{\boldsymbol{m}(t)} \left(\boldsymbol{m}^{\text{data}}(t) - \boldsymbol{m}(\boldsymbol{x},t)\right),$$

then associates J^{data} with a regularization term such as those presented in section 10.2. The problem thus is to minimize the composite criterion

$$J(\boldsymbol{x}) = J^{\text{data}}(\boldsymbol{x}) + J_x(\boldsymbol{x}) \tag{10.25}$$

obtained under the constraints (10.23). Among the references that adopt this approach for processing optical interferometry data, [TGF03] is one of the most noteworthy.

Such works are based on the use of local descent methods. Unfortunately, the criterion J is non-convex. To be more precise, the difficulty of the problem can be summed up in the following three points:

1. the small number of Fourier coefficients makes the problem under-determined: the regularization term can get around this under-determination, e.g. by limiting the high frequencies of the reconstructed object [Lan98];

2. the turbulence implies phase indetermination. This type of indetermination makes the Fourier synthesis problem non-convex and adding a regularization term does not generally correct the problem;

3. finally, the fact that we have phase modulus measurements with Gaussian noise leads to a non-Gaussian likelihood in $\boldsymbol{x}$ and a non-convex log-likelihood. This point, which has long been known in the field of radar was identified only very recently in optical interferometry [MMLB05b]. In other words, even if we had all the complex visibility phase measurements instead of just the closure phases, the data fidelity term would still be non-convex.

These characteristics imply that optimizing J by a local descent algorithm can only work if the initialization puts us in the "right" valley of the criterion. The use of a global optimization algorithm has never been proposed in optical interferometry as far as we know. It would no doubt be useful to explore this path as long as the number of variables remained reasonable, in particular in comparison with the very large dimension maps that are reconstructed in radio interferometry.

10.5.3 Myopic modeling

Another approach is to put the problem in terms of missing data; this is phase data that is eliminated by the use of a closure operator, i.e., elements of the kernel of $\boldsymbol{C}$ (10.21). The *myopic* approach thus consists of finding object $\boldsymbol{x}$ and missing phase data $\boldsymbol{\alpha}$ jointly. This technique is called *self-calibration* in radio-interferometry [CW81] and has enabled reliable images to be reconstructed in situations of partial phase indetermination. The first myopic approaches put forward in optical interferometry were strongly influenced by this work [Lan98]. Recent findings indicate that these transpositions were based on too great a simplification of the measuring procedure belonging to optical interferometry. This section outlines a precise myopic approach applied to OI.

The construction of a myopic model starts from a generalized inverse solution to the phase closure equation of (10.22), using the operator

$$\boldsymbol{C}^\dagger \triangleq \boldsymbol{C}^T \left(\boldsymbol{C}\boldsymbol{C}^T\right)^{-1}.$$

By applying $\boldsymbol{C}^\dagger$ on the left to (10.22) and (10.21) we have

$$\exists \boldsymbol{\alpha}(t) \;\mid\; \boldsymbol{C}^\dagger \boldsymbol{\beta}^{\text{data}}(t) = \boldsymbol{\phi}(\boldsymbol{x},t) + \bar{\boldsymbol{B}}\boldsymbol{\alpha}(t) + \boldsymbol{C}^\dagger \boldsymbol{\beta}^{\text{noise}}(t).$$

It is thus tempting to define a pseudo-equation of visibility phase measurement by identifying the last term of the latter equation with a measurement pseudo-noise:

$$\boldsymbol{\phi}^{\text{data}}(t) = \underbrace{\boldsymbol{\phi}(\boldsymbol{x},t) + \boldsymbol{B}\boldsymbol{\alpha}(t)}_{\boldsymbol{\phi}(\boldsymbol{x},\boldsymbol{\alpha}(t),t)} + \boldsymbol{\phi}^{\text{noise}}(t). \tag{10.26}$$

This approach is similar to that presented in reference [Lan01]. Unfortunately, as matrix $\boldsymbol{C}^\dagger$ is singular, this identification is not rigorously possible and we are led to associate an ad hoc covariance matrix $\boldsymbol{R}_\phi$ with the term $\boldsymbol{\phi}^{\text{noise}}(t)$ so as to approximately fit the statistical behavior of the closures. These problems of covariance approximation are ignored in [Lan01]. The more recent references [Mei05, MM07] discuss the possible choices for $\boldsymbol{R}_\phi$ and propose the use of the following diagonal matrix:

$$\boldsymbol{R}_{\boldsymbol{\phi}} \propto \text{Diag}\left\{\boldsymbol{C}^\dagger \boldsymbol{R}_{\boldsymbol{\beta}} \boldsymbol{C}^{\dagger,T}\right\}$$

where the expression $\text{Diag}\{\boldsymbol{M}\}$ designates the diagonal matrix formed with the diagonal of $\boldsymbol{M}$.

Finding a suitable approximation for the covariance of the amplitude measurements (10.22), see [Mei05, MM07], gives a myopic measurement model, i.e., one that depends on the unknowns $\boldsymbol{x}$ and $\boldsymbol{\alpha}$:

$$\begin{cases} \boldsymbol{a}^{\text{data}}(t) = \boldsymbol{a}(\boldsymbol{x},t) + \boldsymbol{a}^{\text{noise}}(t), & \boldsymbol{a}^{\text{noise}}(t) \sim \mathcal{N}\left(\bar{\boldsymbol{a}}(t), \boldsymbol{R}_{\boldsymbol{a}(t)}\right) \\ \boldsymbol{\phi}^{\text{data}}(t) = \boldsymbol{\phi}(\boldsymbol{x},\boldsymbol{\alpha}(t),t) + \boldsymbol{\phi}^{\text{noise}}(t), & \boldsymbol{\phi}^{\text{noise}}(t) \sim \mathcal{N}\left(\bar{\boldsymbol{\phi}}(t), \boldsymbol{R}_{\boldsymbol{\phi}(t)}\right) \end{cases} \tag{10.27}$$

We now have an explicit model of the phase indetemination noted in section 10.5.2. At this stage, it is possible to envisage using, for example, alternating descent algorithms that successively optimize a regularized criterion coming from (10.27), according to $\boldsymbol{x}$ and $\boldsymbol{\alpha}$. However, it is still true that, as this model is given in modulus and phase, it always leads to a data-fidelity term that is non-convex in $\boldsymbol{x}$, for fixed $\boldsymbol{\alpha}$. Below, we briefly present a convex approximation of this model.

From the pseudo-measurements $\boldsymbol{a}^{\text{data}}(t)$ and $\boldsymbol{\phi}^{\text{data}}(t)$, let us form complex pseudo visibilities

$$\boldsymbol{y}^{\text{data}}(t) \triangleq \boldsymbol{a}^{\text{data}}(t)\, e^{j\boldsymbol{\phi}^{\text{data}}(t)}.$$

The data model is thus

$$\boldsymbol{y}^{\text{data}}(t) = \left(\boldsymbol{a}(\boldsymbol{x},t) + \boldsymbol{a}^{\text{noise}}(t)\right) e^{j\left(\boldsymbol{\phi}(\boldsymbol{x},\boldsymbol{\alpha}(t),t)+\boldsymbol{\phi}^{\text{noise}}(t)\right)}.$$

The noise on these measurements, although additive and Gaussian in modulus and phase separately, is not a complex additive Gaussian noise. In reference [MMLB05a], the authors show how this distribution can be best approximated by an additive Gaussian noise $\boldsymbol{y}^{\text{noise}}(t)$.

with

$$\boldsymbol{y}^{\text{data}}(t) = \boldsymbol{y}(\boldsymbol{x},\boldsymbol{\alpha}(t),t) + \boldsymbol{y}^{\text{noise}}(t) \tag{10.28}$$

$$\boldsymbol{y}(\boldsymbol{x},\boldsymbol{\alpha}(t),t) \triangleq \boldsymbol{a}(\boldsymbol{x},t) e^{\boldsymbol{\phi}(\boldsymbol{x},\boldsymbol{\alpha}(t),t)} \tag{10.29}$$

In general, this approximation leads to a data fitting term J^{pseudo} that is quadratic in the real and imaginary parts of the residuals $y_{k\ell}^{\text{data}}(t) - y_{k\ell}(\boldsymbol{x},\boldsymbol{\alpha}(t),t)$. By associating this term with a convex regularization term, we obtain a composite criterion that is convex in $\boldsymbol{x}$ at fixed $\boldsymbol{\alpha}$. The WISARD algorithm [MM07] makes use of this property by minimizing this composite criterion alternately in $\boldsymbol{x}$ for the current $\boldsymbol{\alpha}$ and in $\boldsymbol{\alpha}$ for the current $\boldsymbol{x}$.

uses a minimization technique alternating in $\boldsymbol{x}$ and $\boldsymbol{\alpha}$ applied to this criterion.

10.5.4 Results

This section presents some results of processing by the WISARD algorithm [MM07] based on the myopic approach described in 10.5.3.

10.5.4.1 Processing of synthetic data

The first example takes synthetic interferometric data that were used in the international Imaging Beauty Contest organized by P. Lawson for the InternationalAstronomical Union (IAU) [LCH+04]. This data simulates the observation of the synthetic object shown in Figure 10.11 with the NPOI [NPO] 6-telescope interferometer. The corresponding frequency coverage, shown in Figure 10.11, has a circular structure typical of the *super-synthesis* technique. We recall that super-synthesis consists of repeating the measurements over several instants of measurement (possibly over several nights of observation) so that the same baselines access different spatial frequencies because of the Earth's rotation. In total, there are 195 square visibility modules and 130 closure phases, together with the associated variances.

Three reconstructions obtained with WISARD are shown in Figure 10.12. On the left is a reconstruction using a quadratic regularization based on a PSD model in $1/|u|^3$ for a weak regularization parameter, in the center a reconstruction with a correct parameter. The latter gives a satisfactory level of smoothing but does not restore the peak

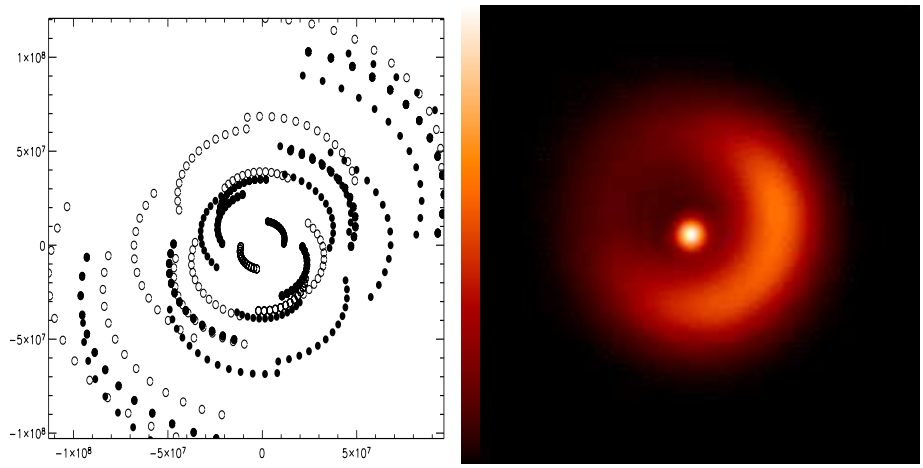

Figure 10.11: Synthetic object (right) and frequency coverage (left) from the Imaging Beauty Contest 2004

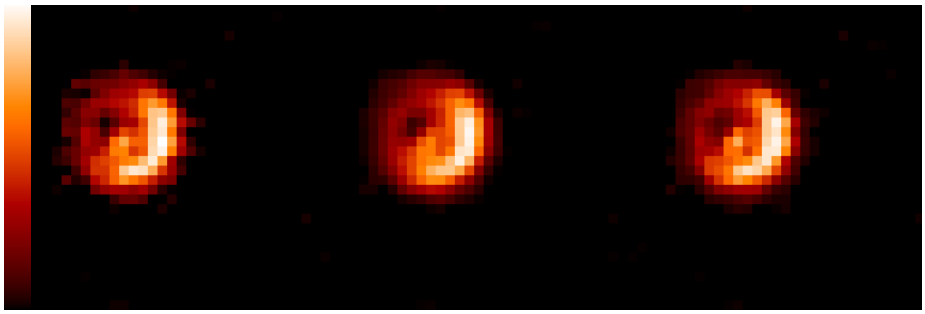

Figure 10.12: Reconstructions with WISARD. Left: under-regularized quadratic model; center: quadratic model with correct regularization parameter; right: white L_2L_1 model of equation (10.8)

in the center of the object. The peak is visible in the under-regularized reconstruction on the left but at the cost of too high a residual variance.

The reconstruction presented on the right is a good trade-off between smoothing and restoration of the central peak thanks to the use of the white prior term introduced in section 10.2. The goodness of fit of the L_2L_1 reconstruction can be appreciated in Figure 10.13. The crosses show the reconstructed visibility moduli (i.e., of the FT of the reconstructed object at the measurement frequencies) and the squares the moduli of the measured visibilities. The difference between the two, weighted by 10 times the standard deviation of the moduli, is shown as the line. The mean value of this difference is 0.1, which shows a good fit, to one standard deviation.

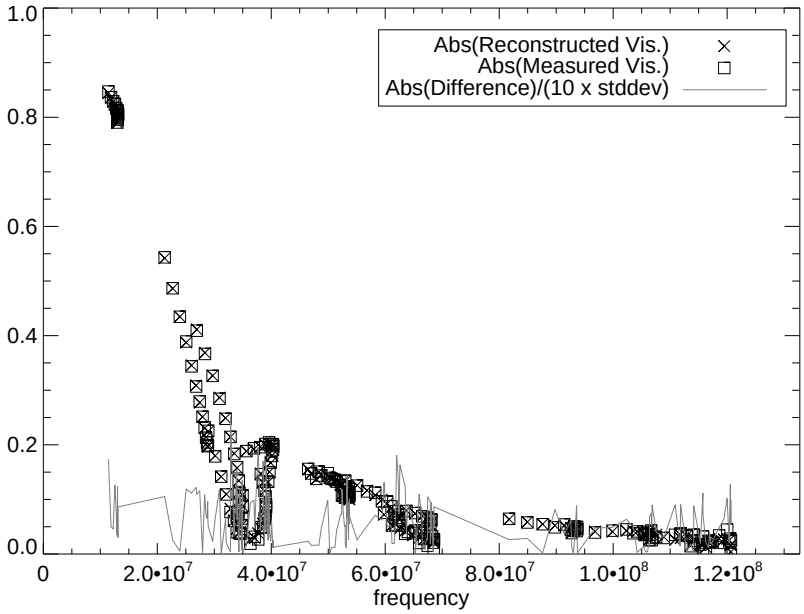

Figure 10.13: Goodness of fit at WISARD convergence

10.5.4.2 Processing of experimental data

Here, we present the reconstruction of the star χ Cygni from experimental data using the WISARD [MM07] algorithm. The data was obtained by S. Lacour and S. Meimon under the leadership of G. Perrin during a measuring campaign on the IOTA interferometer [IOT] in May 2005. As already mentioned, each measurement has to be calibrated by observation of an object that acts as a point source at the instrument's resolving power. The calibrators chosen were HD 180450 and HD 176670.

χ Cygni is a Mira-type star, Mira itself being an example of such stars. Perrin *et al.* [PRM+04] propose a laminar model of Mira-type stars, composed of a photosphere, an empty layer, and a fine molecular layer. The aim of the mission was to obtain images of χ Cygni in the H band (1.65 microns ± 175 nm) and, in particular, to highlight possible dissymmetries in the structure of the molecular layer.

Figure 10.14 shows, on the left, the $u - v$ coverage obtained, i.e., the set of spatial frequencies measured, multiplied by the observation wavelength. As the sky is

habitually represented with the west on the right, the coordinates used are, in fact, $-u, v$. The domain of the accessible $u - v$ plane is constrained by the geometry of the interferometer and the position of the star in the sky. The "hour-glass" shape is characteristic of the IOTA interferometer, and entails non-uniform resolution that affects the image reconstruction, shown on the right. The reconstructed angular field has sides of 30 milliarcseconds. In addition to the positivity constraint, the regularization used is the white L_2L_1 criterion described in section 10.2. The interested reader will find an astrophysical interpretation of this result in [Lac07].

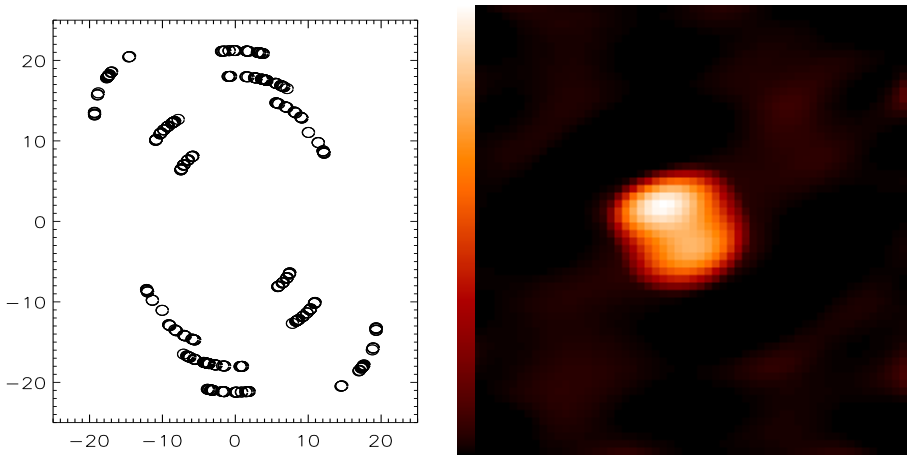

Figure 10.14: Frequency coverage (left) and reconstruction of the star χ Cygni (right)

Bibliography

[AD88] G. R. Ayers and J. C. Dainty. Iterative blind deconvolution and its applications. *Opt. Lett.*, 13:547–549, 1988.

[BBB+96] J. E. Baldwin, M. G. Beckett, R. C. Boysen, D. Burns, D. F. Buscher, G. C. Cox, C. A. Haniff, C. D. Mackay, N. S. Nightingale, J. Rogers, P. A. G. Scheuer, T. R. Scott, P. G. Tuthill, P. J. Warner, D. M. A. Wilson, and R. W. Wilson. The first images from an optical aperture synthesis array: mapping of capella with COAST at two epochs. *Advances in Applied Probability*, 306:L13+, fév. 1996.

[BHE+97] J. A. Benson, D. J. Hutter, N. M. Elias, II, P. F. Bowers, K. J. Johnston, A. R. Hajian, J. T. Armstrong, D. Mozurkewich, T. A. Pauls, L. J. Rickard, C. A. Hummel, N. M. White, D. Black, and C. S. Denison. Multichannel optical aperture synthesis imaging of zeta1 ursae majoris with the navy prototype optical interferometer. *Astron. J.*, 114:1221–1226, sep. 1997.

[BHK+03] J.-P. Berger, P. Haguenauer, P. Y. Kern, K. Rousselet-Perraut, F. Malbet, S. Gluck, L. Lagny, I. Schanen-Duport, E. Laurent, A. Delboulbe, E. Tatulli, W. A. Traub, N. Carleton, R. Millan-Gabet, J. D. Monnier, E. Pedretti, and S. Ragland. An integrated-optics 3-way beam combiner for iota. In *Interferometry for Optical Astronomy II. Edited by Wesley A. Traub . Proceedings of the SPIE, Volume 4838, pp. 1099-1106 (2003).*, pages 1099–1106, fév. 2003.

[BHMW86] J. E. Baldwin, C. A. Haniff, Mackay, and P. J. Warner. Closure phase in high-resolution optical imaging. *Nature (London)*, 320:595–597, avr. 1986.

[BI96] Stéphane Brette and Jérôme Idier. Optimized single site update algorithms for image deblurring. In *Proceedings of the International Conference on Image Processing*, pages 65–68, Lausanne, Suisse, sep. 1996.

[BKL+94] P. A. Bakut, V. E. Kirakosyants, V. A. Loginov, C. J. Solomon, and J. C. Dainty. Optimal wavefront reconstruction from a Shack-Hartmann sensor by use of a Bayesian algorithm. *Opt. Commun.*, 109:10–15, juin 1994.

[BMI03] A. Blanc, L. M. Mugnier, and J. Idier. Marginal estimation of aberrations and image restoration by use of phase diversity. *Journal of the Optical Society of America (A)*, 20(6):1035–1045, 2003.

[BW93] M. Born and E. Wolf. *Principles of Optics*. Pergamon Press, Sixth (corrected) edition, 1993.

[Cas97] F. Cassaing. *Analyse d'un instrument à synthèse d'ouverture optique : méthodes de cophasage et imagerie à haute résolution angulaire*. thèse de doctorat, Université de Paris–Sud, Orsay, déc. 1997.

[CFM+98] J.-M. Conan, T. Fusco, L. M. Mugnier, E. Kersale, and V. Michau. Deconvolution of adaptive optics images with imprecise knowledge of the point spread function results on astronomical objects. In D. Bonaccini, editor, *Astronomy with adaptive optics: present results and future programs*, number 56 in ESO Conf. and Workshop Proc., pages 121–132, Sonthofen, Allemagne, sep. 1998.

[CFM+00] J.-M. Conan, T. Fusco, L. Mugnier, F. Marchis, C. Roddier, and F. Roddier. Deconvolution of adaptive optics images: from theory to practice. In P. Wizinowich, editor, *Adaptive Optical Systems Technology*, volume 4007, pages 913–924, Munich, Allemagne, 2000. Proc. Soc. Photo-Opt. Instrum. Eng.

[CMF+98] J.-M. Conan, L. M. Mugnier, T. Fusco, V. Michau, and G. Rousset. Myopic deconvolution of adaptive optics images using object and point spread function power spectra. *Appl. Opt.*, 37(21):4614–4622, juil. 1998.

[CMLG07] G. Chenegros, L. M. Mugnier, F. Lacombe, and M. Glanc. 3D phase diversity: a myopic deconvolution method for short-exposure images. Application to retinal imaging. *Journal of the Optical Society of America (A)*, 24(5):1349–1357, mai 2007.

[Con94] J.-M. Conan. *Etude de la correction partielle en optique adaptative*. thèse de doctorat, Université de Paris–Sud, Orsay, oct. 1994.

[CR05] J.-M. Conan and G. Rousset, editors. *Multi-Conjugate Adaptive Optics for Very Large Telescopes Dossier*, volume 6 fascicule 10 of *C. R. Physique, Académie des Sciences*. Elsevier, Paris, déc. 2005.

[CRM95] J.-M. Conan, G. Rousset, and P.-Y. Madec. Wave-front temporal spectra in high-resolution imaging through turbulence. *Journal of the Optical Society of America (A)*, 12(12):1559–1570, juil. 1995.

[CW81] T. J. Cornwell and P. N. Wilkinson. A new method for making maps with unstable radio interferometers. *Monthly Notices of the Royal Astronomical Society*, 196:1067–1086, 1981.

[DBF+06] K. Dohlen, J.-L. Beuzit, M. Feldt, D. Mouillet, P. Puget, J. Antichi, A. Baruffolo, P. Baudoz, A. Berton, A. Boccaletti, M. Carbillet, J. Charton, R. Claudi, M. Downing, C. Fabron, P. Feautrier, E. Fedrigo, T. Fusco, J.-L. Gach, R. Gratton, N. Hubin, M. Kasper, M. Langlois, A. Longmore, C. Moutou, C. Petit, J. Pragt, P. Rabou, G. Rousset, M. Saisse, H.-M. Schmid, E. Stadler, D. Stamm, M. Turatto, R. Waters, and F. Wildi. Sphere: A planet finder instrument for the vlt. In I. S McLean and M. Iye, editors, *Ground-based and Airborne Instrumentation for Astronomy*, volume 6269. Proc. Soc. Photo-Opt. Instrum. Eng., 2006.

[Fon85] J.-C. Fontanella. Analyse de surface d'onde, déconvolution et optique active. *J. of Optics (Paris)*, 16(6):257–268, 1985.

[Fri65] D. L. Fried. Statistics of a geometric representation of wavefront distortion. *Journal of the Optical Society of America*, 55(11):1427–1435, 1965.

[FVCM99] T. Fusco, J.-P. Veran, J.-M. Conan, and L. Mugnier. Myopic deconvolution method for adaptive optics images of stellar fields. *Astron. Astrophys. Suppl.*, 134:1–10, jan. 1999.

[GGL+04] M. Glanc, E. Gendron, F. Lacombe, D. Lafaille, J.-F. Le Gargasson, and P.Léna. Towards wide-field retinal imaging with adaptive optics. *Opt. Commun.*, 230:225–238, 2004.

[Gla02] M. Glanc. *Applications Ophtalmologiques de l'Optique Adaptative*. PhD thesis, Univ. Paris XI, 2002.

[Gon76] R. A. Gonsalves. Phase retrieval from modulus data. *Journal of the Optical Society of America*, 66(9):961–964, 1976.

[Gon82] R. A. Gonsalves. Phase retrieval and diversity in adaptive optics. *Optical Engineering*, 21(5):829–832, 1982.

[Goo68] J. W. Goodman. *Introduction to Fourier Optics*. McGraw-Hill, New York, 1968.

[Goo85] Joseph W. Goodman. *Statistical optics*. John Wiley, New York, 1985.

[GRM+06] D. Gratadour, D. Rouan, L. M. Mugnier, T. Fusco, Y. Clénet, E. Gendron, and F. Lacombe. Near-IR AO dissection of the core of NGC 1068 with NaCo. *Astron. Astrophys.*, 446(3):813–825, fév. 2006.

[GS72a] R. W. Gerchberg and W. O. Saxton. A practical algorithm for the determination of phase from image and diffraction plane pictures. *Optik*, 35:237–246, 1972.

[GS72b] R. W. Gerchberg and W. O. Saxton. A practical algorithm for the determination of phase from image and diffraction plane pictures. *Optik*, 35:237–246, 1972.

[HMT+87] C. A. Haniff, C. D. Mackay, D. J. Titterington, D. Sivia, and J. E. Baldwin. The first images from optical aperture synthesis. *Nature (London)*, 328:694–696, août 1987.

[Hol92] T. J. Holmes. Blind deconvolution of speckle images quantum-limited incoherent imagery: maximum-likehood approach. *Journal of the Optical Society of America (A)*, 9(7):1052– 1061, 1992.

[HS04] J. M. Hill and P. Salinari. The large binocular telescope project. In J. M. Oschmann, Jr., editor, *Ground-based Telescopes. Edited by Oschmann, Jacobus M., Jr. Proceedings of the SPIE, Volume 5489, pp. 603-614 (2004).*, volume 5489 of *Presented at the Society of Photo-Optical Instrumentation Engineers (SPIE) Conference*, pages 603–614, oct. 2004.

[IMB05] J. Idier, L. Mugnier, and A. Blanc. Statistical behavior of joint least square estimation in the phase diversity context. *Inverse Problems*, 14(12):2107–2116, déc. 2005.

[IOT] http://tdc-www.harvard.edu/iota/.

[JC93] S. M. Jefferies and J. C. Christou. Restoration of astronomical images by iterative blind deconvolution. *Astrophys. J.*, 415:862–874, 1993.

[Jen58] R. C. Jennison. A phase sensitive interferometer technique for the measurement of the fourier transforms of spatial brightness distribution of small angular extent. *Monthly Notices of the Royal Astronomical Society*, 118:276–284, 1958.

[Kec] http://www.keckobservatory.org/.

[KRP+06] C. Kulcsár, H.-F. Raynaud, C. Petit, J.-M. Conan, and P. Viaris de Lesegno. Optimal control, observers and integrators in adaptive optics. *Opt. Express*, 14(17):7464–7476, 2006.

[KT74] K. T. Knox and B. J. Thompson. Recovery of images from atmospherically degraded short exposure photographs. *Astrophys. J. Lett.*, 193:L45–L48, 1974.

[Lab70] A. Labeyrie. Attainment of diffraction-limited resolution in large telescopes by Fourier analysing speckle patterns. *Astronomy and Astrophysics*, 6:85–87, 1970.

[Lab75] A. Labeyrie. Interference fringes obtained on VEGA with two optical telescopes. *Astrophys. J. Lett.*, 196:L71–L75, mars 1975.

[Lac07] S. Lacour. *Imagerie des étoiles évoluées par interférométrie. Réarrangement de pupille*. PhD thesis, Univ. Paris VI, 2007.

[Lan92] R. G. Lane. Blind deconvolution of speckle images. *Journal of the Optical Society of America (A)*, 9(9):1508–1514, 1992.

[Lan96] R. G. Lane. Methods for maximum-likelihood deconvolution. *Journal of the Optical Society of America (A)*, 13(10):1992–1998, 1996.

[Lan98] A. Lannes. Weak-phase imaging in optical interferometry. *Journal of the Optical Society of America (A)*, 15(4):811–824, avr. 1998.

[Lan01] A. Lannes. Integer ambiguity resolution in phase closure imaging. *Optical Society of America Journal A*, 18:1046–1055, mai 2001.

[Law97] P. R. Lawson, editor. *Long baseline stellar interferometry*, 1997.

[LCH+04] P. R. Lawson, W. D. Cotton, C. A. Hummel, J. D. Monnier, M. Zhao, J. S. Young, H. Thorsteinsson, S. C. Meimon, L. Mugnier, G. Le Besnerais, E. Thiébaut, and P. G. Tuthill. An interferometric imaging beauty contest. In Wesley A. Traub, editor, *New frontiers in stellar interferometry*, volume 5491, pages 886–899. Proc. Soc. Photo-Opt. Instrum. Eng., 2004.

[LRCK+04] B. Le Roux, J.-M. Conan, C. Kulcsár, H.-F. Raynaud, L. M. Mugnier, and T. Fusco. Optimal control law for classical and multiconjugate adaptive optics. *Journal of the Optical Society of America (A)*, 21(7), juil. 2004.

[Mar89] J.-M. Mariotti. Introduction to Fourier optics and coherence. In D. M. Alloin and J.-M. Mariotti, editors, *Diffraction-limited imaging with very large telescopes*, volume 274 of *NATO ASI Series C*, pages 3–31. Kluwer Academic Publishers, Cargese, 1989.

[MBI06] L. M. Mugnier, A. Blanc, and J. Idier. Phase diversity: a technique for wave-front sensing and for diffraction-limited imaging. In Peter Hawkes, editor, *Advances in Imaging and Electron Physics*, volume 141, chapter 1, pages 1–76. Elsevier, 2006.

[Mei05] S. Meimon. *Reconstruction d'images astronomiques en interférométrie optique*. PhD thesis, Université Paris Sud, 2005.

[Mer88] F. Merkle, editor. *High-resolution imaging by interferometry, part II*, number 29 in ESO Conference and Workshop Proceedings, Garching bei München, Allemagne, juil. 1988.

[MFC04] L. M. Mugnier, T. Fusco, and J.-M. Conan. MISTRAL: a myopic edge-preserving image restoration method, with application to astronomical adaptive-optics-corrected long-exposure images. *Journal of the Optical Society of America (A)*, 21(10):1841–1854, oct. 2004.

[Mic91] A. A. Michelson. Measurement of Jupiter's satellites by interference. *Nature (London)*, 45:160–161, déc. 1891.

[MM07] L. Mugnier and S. Meimon. WISARD software documentation. Technical report, ONERA, 2007. European Interferometry Initiative, Joint Research Action 4, 6th Framework Programme of the EU.

[MMLB05a] S. Meimon, L. M. Mugnier, and G. Le Besnerais. Reconstruction method for weak-phase optical interferometry. *Opt. Lett.*, 30(14):1809–1811, juil. 2005.

[MMLB05b] S. Meimon, L. M. Mugnier, and Guy Le Besnerais. A convex approximation of the likelihood in optical interferometry. *Journal of the Optical Society of America (A)*, nov. 2005.

[Mon03] J. D. Monnier. Optical interferometry in astronomy. *Reports of Progress in Physics*, 66:789–857, mai 2003.

[MP21] A. A. Michelson and F. G. Pease. Measurement of the diameter of alpha Orionis with the interferometer. *Astrophys. J.*, 53:249–259, mai 1921.

[MRC+01] L. M. Mugnier, C. Robert, J.-M. Conan, V. Michau, and S. Salem. Myopic deconvolution from wavefront sensing. *Journal of the Optical Society of America (A)*, 18:862–872, avr. 2001.

[MTBB+94] D. Mourard, I. Tallon-Bosc, A. Blazit, D. Bonneau, G. Merlin, F. Morand, F. Vakili, and A. Labeyrie. The GI2T interferometer on Plateau de Calern. *Advances in Applied Probability*, 283:705–713, mars 1994.

[Nol76] R. J. Noll. Zernike polynomials and atmospheric turbulence. *Journal of the Optical Society of America*, 66(3):207–211, 1976.

[NPO] http://ftp.nofs.navy.mil/projects/npoi/.

[PCK+05] C. Petit, J.-M. Conan, C. Kulcsar, H.-F. Raynaud, T. Fusco, J. Montri, and D. Rabaud. Optimal control for multi-conjugate adaptive optics. *C. R. Physique*, 6(10):1059–1069, 2005.

[PRF88] J. Primot, G. Rousset, and J.-C. Fontanella. Image deconvolution from wavefront sensing atmospheric turbulence simulation cell results. In Merkle [Mer88], pages 683–692.

[PRF90] J. Primot, G. Rousset, and J.-C. Fontanella. Deconvolution from wavefront sensing a new technique for compensating turbulence-degraded images. *Journal of the Optical Society of America (A)*, 7(9):1598–1608, 1990.

[PRM+04] G. Perrin, S.T. Ridgway, B. Mennesson, W.D. Cotton, J. Woillez, T. Verhoelst, P. Schuller, V. Coudé du Foresto, W.A. Traub, R. Millan-Galbet, and M.G. Lacasse. Unveiling mira stars behind the molecules. confirmation of the molecular layer model with narrow band near-infrared interferometry. *Astron. Astrophys.*, 426:279–296, oct. 2004.

[PWL+06] G. Perrin, J. Woillez, O. Lai, J. Guérin, T. Kotani, P. L. Wizinowich, D. Le Mignant, M. Hrynevych, J. Gathright, P. Léna, F. Chaffee, S. Vergnole, L. Delage, F. Reynaud, A. J. Adamson, C. Berthod, B. Brient, C. Collin, J. Crétenet, F. Dauny, C. Deléglise, P. Fédou, T. Goeltzenlichter, O. Guyon, R. Hulin, C. Marlot, M. Marteaud, B.-T. Melse, J. Nishikawa, J.-M. Reess, S. T. Ridgway, F. Rigaut, K. Roth, A. T. Tokunaga, and D. Ziegler. Interferometric coupling of the Keck telescopes with single-mode fibers. *Science*, 311:194–+, jan. 2006.

[Rey83] William J.J. Rey. *Introduction to robust and quasi-robust statistical methods*. Springer-Verlag, Berlin, 1983.

[RFK+90] G. Rousset, J.-C. Fontanella, P. Kern, P. Gigan, F. Rigaut, P. Lena, C. Boyer, P. Jagourel, J.-P. Gaffard, and F. Merkle. First diffraction-limited astronomical images with adaptive optics. *Astronomy and Astrophysics*, 230:29–32, 1990.

[RGL82] F. Roddier, J. M. Gilli, and G. Lund. On the origin of speckle boiling and its effects in stellar speckle interferometry. *J. of Optics (Paris)*, 13(5):263–271, 1982.

[RMCS01] G. Rousset, L. M. Mugnier, F. Cassaing, and B. Sorrente. Imaging with multi-aperture optical telescopes and an application. *C. R. Acad. Sci. Paris*, série IV, tome 2(1):17–25, jan. 2001.

[Rod81] F. Roddier. The effects of atmospherical turbulence in optical astronomy. In E. Wolf, editor, *Progress in Optics*, volume XIX, pages 281–376. North Holland, Amsterdam, 1981.

[Rod88a] F. Roddier. Curvature sensing and compensation a new concept in adaptive optics. *Appl. Opt.*, 27(7):1223–1225, avr. 1988.

[Rod88b] F. Roddier. Passive versus active methods in optical interferometry. In Merkle [Mer88], pages 565–574.

[Rod90] N. Roddier. Atmospheric wavefront simulation using Zernike polynomials. *Optical Engineering*, 29(10):1174–1180, 1990.

[Rod99] F. Roddier, editor. *Adaptive Optics in Astronomy*. Cambridge Univ. Press, Cambridge, 1999.

[Rou99] G. Rousset. Wave-front sensors. In Roddier [Rod99], chapter 5, pages 91–130.

[RRG+98] F. Roddier, C. Roddier, J. E. Graves, M. J. Northcott, and T. Owen. Neptune cloud structure and activity: Ground based monitoring with adaptive optics. *Icarus*, 136:168–172, 1998.

[Sch93] T. J. Schulz. Multiframe blind deconvolution of astronomical images. *Journal of the Optical Society of America (A)*, 10(5):1064–1073, 1993.

[SM85] R. J. Sasiela and J. G. Mooney. An optical phase reconstructor based on using a multiplier-accumulator approach. In *Proc. Soc. Photo-Opt. Instrum. Eng.*, volume 551, pages 170–176. Proc. Soc. Photo-Opt. Instrum. Eng., 1985.

[SP71] R. B. Shack and B. C. Plack. Production and use of a lenticular Hartmann screen (abstract). *Journal of the Optical Society of America*, 61:656, 1971.

[TC95] E. Thiebaut and J.-M. Conan. Strict *a priori* constraints for maximum-likelihood blind deconvolution. *Journal of the Optical Society of America (A)*, 12(3):485–492, 1995.

[TGF03] E. Thiébaut, P. J. V. Garcia, and R. Foy. Imaging with Amber/VLTI: the case of microjets. *Astrophys. Space. Sci.*, 286:171–176, 2003.

[Ver97] J.-P. Veran. *Estimation de la réponse impulsionnelle et restauration d'image en optique adaptative. Application au système d'optique adaptative du Télescope Canada-France-Hawaii*. thèse de doctorat, ENST, Paris, nov. 1997.

[VRMR97] J.-P. Veran, F. Rigaut, H. Maitre, and Daniel Rouan. Estimation of the adaptive optics long exposure point spread function using control loop data. *Journal of the Optical Society of America (A)*, 14(11):3057–3069, 1997.

[Wal83] E. P. Wallner. Optimal wave-front correction using slope measurements. *Journal of the Optical Society of America (A)*, 73(12):pp 1771–1776, déc. 1983.

[Wei77] G. Weigelt. Modified astronomical speckle interferometry “speckle masking”. *Opt. Commun.*, 21(1):55–59, 1977.